Title

Beamspace dual signal space projection (bDSSP): a method for selective detection of deep sources in MEG measurements

Journal

Journal of Neural Engineering, 15(3)

ISSN

1741-2560

Authors

Sekihara, Kensuke

Adachi, Yoshiaki

Kubota, Hiroshi K

et al.

Publication Date

2018-06-01

DOI

10.1088/1741-2552/aab5bd

Peer reviewed

HHS Public Access

Author manuscript

J Neural Eng. Author manuscript; available in PMC 2018 December 10.

Published in final edited form as:

J Neural Eng. 2018 June ; 15(3): 036026. doi:10.1088/1741-2552/aab5bd.

Beamspace dual signal space projection (bDSSP): a method for selective detection of deep sources in MEG measurements

Kensuke Sekihara[1,2], **Yoshiaki Adachi**[3], **Hiroshi K Kubota**[4], **Chang Cai**[5], and **Srikantan S Nagarajan**[5]

[1]Signal Analysis Inc., Hachioji, Tokyo, Japan

[2]Department of Advanced Technology in Medicine, Tokyo Medical and Dental University, 1-5-45 Yushima, Bunkyo-ku, Tokyo 113-8519, Japan

[3]Applied Electronics Laboratory, Kanazawa Institute of Technology, Kanazawa, Japan

[4]Healthcare Business Center, Business Development Division, Ricoh Ltd., Tokyo, Japan

[5]Biomagnetic Imaging Laboratory, University of California, San Francisco, 513 Parnassus Avenue, S362, San Francisco, CA 94143, United States of America

Abstract

Objective.—Magnetoencephalography (MEG) has a well-recognized weakness at detecting deeper brain activities. This paper proposes a novel algorithm for selective detection of deep sources by suppressing interference signals from superficial sources in MEG measurements.

Approach.—The proposed algorithm combines the beamspace preprocessing method with the dual signal space projection (DSSP) interference suppression method. A prerequisite of the proposed algorithm is prior knowledge of the location of the deep sources. The proposed algorithm first derives the basis vectors that span a local region just covering the locations of the deep sources. It then estimates the time-domain signal subspace of the superficial sources by using the projector composed of these basis vectors. Signals from the deep sources are extracted by projecting the row space of the data matrix onto the direction orthogonal to the signal subspace of the superficial sources.

Main results.—Compared with the previously proposed beamspace signal space separation (SSS) method, the proposed algorithm is capable of suppressing much stronger interference from superficial sources. This capability is demonstrated in our computer simulation as well as experiments using phantom data.

Significance.—The proposed bDSSP algorithm can be a powerful tool in studies of physiological functions of midbrain and deep brain structures.

Keywords

neuromagnetism; deep sources; electromagnetic brain imaging; magnetoencephalography (MEG); source localization; MEG source space analysis

k-sekihara@nifty.com.

1. Introduction

Electrophysiological activity of neurons in the cerebral cortex generates weak but detectable magnetic fields outside the scalp, and direct non-invasive measurements of these neuronal activities can be achieved with magnetoencephalography (MEG) [1–3]. Modern MEG systems, combining large-scale sensor arrays with advanced signal processing algorithms, are now capable of imaging dynamic brain activities with the temporal resolution on the order of submilli-seconds.

In spite of its success, MEG has the well-recognized weakness that it is not generally good at detecting deep brain activities, although there have been many attempts on recording MEG signals from deep brain regions [4] such as the thalamus [5–9], amygdala [10, 11], and cerebellum [12, 13]. This is primarily because MEG sensor arrays generally have very low sensitivity near deep brain regions, due to the physical nature of magnetic signals. That is, since magnetic signals attenuate with the inverse-square-distance law, MEG signals arising from deep sources become significantly weaker than signals from superficial cortical sources. Also, it is generally true that when a deeper brain region is active, superficial cortical regions are simultaneously active. In such cases, the activity at a deep brain region is masked by overlapped cortical activities, and only these cortical activities are detected by MEG.

To overcome this weakness, Özkurt *et al* proposed a method of decomposing MEG signals into components corresponding to deep and superficial sources [14]. Their method is based on the signal space separation (SSS) algorithm, which utilizes the vector spherical harmonics expansions of the measured magnetic field [15, 16]. Their method combines the SSS algorithm with so-called beamspace processing [17, 18]. The method proposed by Özkurt *et al* is thus referred to as the beamspace SSS method herein.

The beamspace processing was originally developed to reduce the data dimensionality. Many popular source localization methods, such as the MUSIC algorithm [19, 20] and adaptive beamforming [21, 22], make use of second-order statistics of the measured data. To obtain stable data statistics, a large number of time samples are generally needed, and the number of required time samples linearly increases as the data dimension increases. The beamspace processing was developed to reduce this data-sample requirements by reducing the data dimensionality. The data-dimensionality reduction is achieved by projecting the data vector onto a low-dimensional subspace [22, 23]. In this paper, the beamspace idea is used for preprocessing the data by selective interference cancellation. A brief introduction on the beamspace preprocessing is presented in section 3.1 of this paper.

Inspired by Özkurt *et al*, this paper proposes a novel algorithm for selective detection of a deep source by suppressing interference signals from superficial sources. The proposed method is a combination of the beamspace processing with the previously-proposed interference suppression method called dual signal space projection (DSSP) [24]. Thus, the proposed method is here called beamspace DSSP (bDSSP). Compared with the beamspace SSS, the proposed bDSSP algorithm is capable of suppressing much stronger interference

from superficial sources. This capability is demonstrated in our computer simulation and experiments using phantom data.

This paper is organized as follows: following concise explanations of the DSSP algorithm in section 2, the proposed beamspace DSSP algorithm is described in section 3. We present computer simulations that test the effectiveness of the bDSSP algorithm. In section 5.1, results of experiments using an MEG phantom are presented to further demonstrate the effectiveness of the proposed method. In sections 6 and 7, additional supplementary arguments are presented, including a comparison between the beamspace SSS and bDSSP methods.

2. Dual signal subspace projection algorithm

2.1. Data model

Biomagnetic measurements are usually conducted using a sensor array, which simultaneously measures the biomagn-etic signal with multiple sensors. Let us define the measurement of the mth sensor at time t as $y_m(t)$. The measurement from the whole sensor array is expressed as a column vector $\boldsymbol{y}(t)$: $\boldsymbol{y}(t) = [y_1(t), y_2(t),\ldots, y_M(t)]^T$, which is called the data vector. Here, M is the number of sensors, and the superscript T indicates the matrix transpose. Throughout this paper, plain italics indicate scalars, lower-case boldface italics indicate vectors, and upper-case boldface italics indicate matrices.

Let us assume that a unit-magnitude source exists at $\boldsymbol{r}$ ($\boldsymbol{r} = (x, y, z)$). When this unit-magnitude source is directed in the x, y, and z directions, the outputs of the m-th sensor are respectively denoted as $l_m^x(\boldsymbol{r})$, $l_m^{\boldsymbol{y}}(\boldsymbol{r})$, and $l_m^z(\boldsymbol{r})$. Let us define an $M \times 3$ matrix $\boldsymbol{L}(\boldsymbol{r})$ whose mth row is equal to a 1×3 row vector $\left[l_m^x(\boldsymbol{r}), l_m^y(\boldsymbol{r}), l_m^z(\boldsymbol{r})\right]$. This matrix $\boldsymbol{L}(\boldsymbol{r})$, referred to as the lead field matrix [1, 25], represents the sensitivity of the sensor array at $\boldsymbol{r}$.

The DSSP algorithm was proposed in order to remove interfering magnetic fields overlapped onto signal magnetic fields. The algorithm assumes the data model:

$$\boldsymbol{y}(t) = \boldsymbol{y}_{\mathrm{S}}(t) + \boldsymbol{y}_{\mathrm{I}}(t) + \varepsilon, \quad (1)$$

where $\boldsymbol{y}_{\mathrm{S}}(t)$, (called the signal vector), represents the signal of interest, $\boldsymbol{y}_{\mathrm{I}}(t)$, (called the interference vector), represents the interference magnetic field, and ε, (called the random vector), represents additive sensor noise. We denote the time series outputs of a sensor array $\boldsymbol{y}(t_1),\ldots, \boldsymbol{y}(t_K)$, where K is the total number of measured time points. The measured data matrix $\boldsymbol{B}$ is thus defined as:

$$\boldsymbol{B} = \left[\boldsymbol{y}(t_1), \ldots, \boldsymbol{y}(t_K)\right]. \quad (2)$$

The signal matrix is defined as

$$\boldsymbol{B}_{\mathrm{S}} = \left[\boldsymbol{y}_{\mathrm{S}}(t_1), \ldots, \boldsymbol{y}_{\mathrm{S}}(t_K)\right], \quad (3)$$

and the interference matrix as

$$\boldsymbol{B}_{\mathrm{I}} = \left[\boldsymbol{y}_{\mathrm{I}}(t_1), \ldots, \boldsymbol{y}_{\mathrm{I}}(t_K)\right]. \quad (4)$$

Then, the data model in equation (1) is expressed in a matrix form as:

$$\boldsymbol{B} = \boldsymbol{B}_{\mathrm{S}} + \boldsymbol{B}_{\mathrm{I}} + \boldsymbol{B}_{\boldsymbol{\varepsilon}}, \quad (5)$$

where $\boldsymbol{B}_{\boldsymbol{\varepsilon}}$ is the noise matrix whose j-th column is equal to the noise vector $\boldsymbol{\varepsilon}$ at time t_j.

2.2. Pseudo-signal subspace projector

The DSSP algorithm assumes the data model in equation (5) with the assumption that the interference sources are located outside the source space[6]. The DSSP algorithm uses the so-called pseudo-signal subspace projector, and to derive it, voxels are defined over the source space, in which the voxel locations are denoted $\boldsymbol{r}_1, \ldots, \boldsymbol{r}_N$. The augmented leadfield matrix over these voxel locations is defined as

$$\boldsymbol{F} = \left[\boldsymbol{L}(\boldsymbol{r}_1), \ldots, \boldsymbol{L}(\boldsymbol{r}_N)\right], \quad (6)$$

and the pseudo-signal subspace $\breve{\mathscr{E}}_{\mathrm{S}}$ is defined such that

$$\breve{\mathscr{E}}_{\mathrm{S}} = \mathrm{csp}(\boldsymbol{F}), \quad (7)$$

where the notation $\mathrm{csp}(\boldsymbol{X})$ indicates the column space of a matrix $\boldsymbol{X}$. If the voxel interval is sufficiently small and voxel discretization errors are negligible, we have the relationship $\breve{\mathscr{E}}_{\mathrm{S}} \supset \mathscr{E}_{\mathrm{S}}$ where $\mathscr{E}_{\mathrm{S}}$ indicates the true signal subspace. Therefore, a vector contained in the signal subspace is also contained in the pseudo-signal subspace.

Let us derive the orthonormal basis vectors of the pseudosignal subspace. To do so, we compute the singular value decomposition of $\boldsymbol{F}$:

$$\boldsymbol{F} = \sum_{j=1}^{M} \lambda_j \boldsymbol{e}_j \boldsymbol{f}_j^T. \quad (8)$$

[6]The source space indicates a region in which signal sources can exist. For example, the entire brain (or entire cortex) is considered as the source space in most MEG measurements.

Note that $\boldsymbol{F}$ is an $M \times N$ matrix, so $\boldsymbol{e}_j$ is an $M \times 1$ column vector and $\boldsymbol{f}_j$ is an $N \times 1$ column vector. In equation (8), we assume the relationship $M < N$, and the singular values are numbered in decreasing order. If the singular values $\lambda_1, \ldots, \lambda_\tau$ are distinctively large and other singular values $\lambda_{\tau+1}, \ldots, \lambda_M$ are nearly equal to zero, the leading τ singular vectors $\boldsymbol{e}_1, \ldots, \boldsymbol{e}_\tau$ form orthonormal basis vectors of the pseudo-signal subspace $\breve{\mathscr{E}}_{\mathrm{S}}$ [26]. Thus, the projector onto $\breve{\mathscr{E}}_{\mathrm{S}}$ is obtained using

$$\breve{\boldsymbol{P}}_S = [\boldsymbol{e}_1, \ldots, \boldsymbol{e}_\tau][\boldsymbol{e}_1, \ldots, \boldsymbol{e}_\tau]^T . \quad (9)$$

Note that, since $\breve{\mathscr{E}}_{\mathrm{S}} \supset \mathscr{E}_{\mathrm{S}}$, the orthogonal projector $(\boldsymbol{I} - \breve{\boldsymbol{P}}_{\mathrm{S}})$ removes the signal vector, i.e. $(\boldsymbol{I} - \breve{\boldsymbol{P}}_{\mathrm{S}})\boldsymbol{y}_{\mathrm{S}}(t) = (\boldsymbol{I} - \breve{\boldsymbol{P}}_{\mathrm{S}})\boldsymbol{B}_{\mathrm{S}} = 0$.

2.3. DSSP algorithm

A detailed explanation of the DSSP algorithm in the context of the time-domain signal subspace can be found in [27]. The DSSP algorithm applies $\breve{\boldsymbol{P}}_{\mathrm{S}}$ and $\boldsymbol{I} - \breve{\boldsymbol{P}}_{\mathrm{S}}$ to the data matrix $\boldsymbol{B}$ to create two kinds of data matrices:

$$\breve{\boldsymbol{P}}_{\mathrm{S}}\boldsymbol{B} = \boldsymbol{B}_{\mathrm{S}} + \breve{\boldsymbol{P}}_{\mathrm{S}}\boldsymbol{B}_{\mathrm{I}} + \breve{\boldsymbol{P}}_{\mathrm{S}}\boldsymbol{B}_{\boldsymbol{\varepsilon}}, \quad (10)$$

$$(\boldsymbol{I} - \breve{\boldsymbol{P}}_{\mathrm{S}})\boldsymbol{B} = (\boldsymbol{I} - \breve{\boldsymbol{P}}_{\mathrm{S}})\boldsymbol{B}_{\mathrm{I}} + (\boldsymbol{I} - \breve{\boldsymbol{P}}_{\mathrm{S}})\boldsymbol{B}_{\boldsymbol{\varepsilon}} . \quad (11)$$

To derive equations (10) and (11), we use $\breve{\boldsymbol{P}}_{\mathrm{S}}\boldsymbol{B}_{\mathrm{S}} = \boldsymbol{B}_{\mathrm{S}}$ and $(\boldsymbol{I} - \breve{\boldsymbol{P}}_{\mathrm{S}})\boldsymbol{B}_{\mathrm{S}} = 0$. Let us use the notation $\mathrm{rsp}(\boldsymbol{X})$ to indicate the row space of a matrix $\boldsymbol{X}$. Then, according to the arguments in [27], the following relationships hold:

$$\mathrm{rsp}(\breve{\boldsymbol{P}}_{\mathrm{S}}\boldsymbol{B}) \subset \mathrm{rsp}(\boldsymbol{B}_{\mathrm{S}}) + \mathrm{rsp}(\breve{\boldsymbol{P}}_{\mathrm{S}}\boldsymbol{B}_{\mathrm{I}}) + \mathrm{rsp}(\breve{\boldsymbol{P}}_{\mathrm{S}}\boldsymbol{B}_{\boldsymbol{\varepsilon}}), \quad (12)$$

$$\mathrm{rsp}((\boldsymbol{I} - \breve{\boldsymbol{P}}_{\mathrm{S}})\boldsymbol{B}) \subset \mathrm{rsp}((\boldsymbol{I} - \breve{\boldsymbol{P}}_{\mathrm{S}})\boldsymbol{B}_{\mathrm{I}}) + \mathrm{rsp}((\boldsymbol{I} - \breve{\boldsymbol{P}}_{\mathrm{S}})\boldsymbol{B}_{\boldsymbol{\varepsilon}}) . \quad (13)$$

Since the relationships, $\mathrm{rsp}(\breve{\boldsymbol{P}}_{\mathrm{S}}\boldsymbol{B}_{\mathrm{I}}) = \mathscr{K}_{\mathrm{I}}$ and $\mathrm{rsp}(\boldsymbol{I} - \breve{\boldsymbol{P}}_{\mathrm{S}})\boldsymbol{B}_{\mathrm{I}} = \mathscr{K}_{\mathrm{I}}$, hold, equations (12) and (13) lead to the relationships:

$$\mathrm{rsp}(\breve{\boldsymbol{P}}_{\mathrm{S}}\boldsymbol{B}) \subset \mathscr{K}_{\mathrm{S}} + \mathscr{K}_{\mathrm{I}} + \breve{\mathscr{K}}_{\varepsilon}, \quad (14)$$

$$\mathrm{rsp}\left(\left(\boldsymbol{I}-\check{\boldsymbol{P}}_{\mathrm{S}}\right)\boldsymbol{B}\right)\subset\mathscr{K}_{\mathrm{I}}+\check{\mathscr{K}}'_{\varepsilon}, \quad (15)$$

Where $\mathscr{K}_{\mathrm{S}}$ and $\mathscr{K}_{\mathrm{I}}$ respectively indicate the time-domain signal and interference subspaces. Here, we use the notations, $\mathrm{rsp}\left(\check{\boldsymbol{P}}_{\mathrm{S}}\boldsymbol{B}_{\boldsymbol{\varepsilon}}\right)=\check{\mathscr{K}}_{\varepsilon}$ and $\mathrm{rsp}\left(\left(\boldsymbol{I}-\check{\boldsymbol{P}}_{\mathrm{S}}\right)\boldsymbol{B}_{\boldsymbol{\varepsilon}}\right)=\check{\mathscr{K}}'_{\varepsilon}$.

Using equations (14) and (15), we can finally derive the relationship [27]:

$$\mathscr{K}_{\mathrm{I}}\supset\mathrm{rsp}\left(\check{\boldsymbol{P}}_{\mathrm{S}}\boldsymbol{B}\right)\cap\mathrm{rsp}\left(\left(\boldsymbol{I}-\check{\boldsymbol{P}}_{\mathrm{S}}\right)\boldsymbol{B}\right). \quad (16)$$

The equation above shows that the intersection between $\mathrm{rsp}\left(\check{\boldsymbol{P}}_{S}\boldsymbol{B}\right)$ and $\mathrm{rsp}\left(\left(\boldsymbol{I}-\check{\boldsymbol{P}}_{\mathrm{S}}\right)\boldsymbol{B}\right)$ forms a subset of the interference subspace $\mathscr{K}_{\mathrm{I}}$. Once the orthonormal basis vectors of the intersection $\psi_1\ldots,\ \psi_r$ are obtained, we can compute the projector onto the intersection $\boldsymbol{\Pi}_{isc}$ such that

$$\boldsymbol{\Pi}_{isc}=\left[\psi_1,\ldots,\psi_r\right]\left[\psi_1,\ldots,\psi_r\right]^T. \quad (17)$$

Using this $\boldsymbol{\Pi}_{isc}$ as the projector onto the interference subspace $\mathscr{K}_{\mathrm{I}}$, the interference removal is achieved and the signal matrix is estimated such that

$$\hat{\boldsymbol{B}}_{S}=\boldsymbol{B}\left(\boldsymbol{I}-\boldsymbol{\Pi}_{isc}\right)=\boldsymbol{B}\left(\boldsymbol{I}-\left[\psi_1,\ldots,\psi_r\right]\left[\psi_1,\ldots,\psi_r\right]^T\right). \quad (18)$$

The method of removing the interference in a manner described above is called DSSP [24]. Note that since the basis vectors of the intersection, $\psi_1\ldots,\ \psi_r$, span only a subset of the interference subspace $\mathscr{K}_{\mathrm{I}}$, this method cannot perfectly remove interferences. However, when the intersection $\mathrm{rsp}\left(\check{\boldsymbol{P}}_{\mathrm{S}}\boldsymbol{B}\right)\cap\mathrm{rsp}\left(\left(\boldsymbol{I}-\check{\boldsymbol{P}}_{\mathrm{S}}\right)\boldsymbol{B}\right)$ is a reasonable approximation of $\mathscr{K}_{\mathrm{I}}$, interferences can effectively be removed by the DSSP algorithm.

3. Beamspace dual signal subspace projection (bDSSP) algorithm

3.1. Beamspace processing

Beamspace processing refers to a signal processing algorithm used for data-dimensionality reduction. Such data-dimensionality reduction is achieved by projecting the data vector onto a low-dimensional subspace. In other words, an $M\times 1$ data vector $\boldsymbol{y}(t)$ is represented with known basis vectors $\boldsymbol{u}_1,\ldots,\boldsymbol{u}_P$, where the number of basis vectors P is smaller than the dimension of the data vector M. That is, if $\boldsymbol{y}(t)$ is expressed using a linear combination of a set of known P basis vectors such that

$$\boldsymbol{y}(t) \approx \sum_{j=1}^{P} c_j(t)\boldsymbol{u}_j, \quad (19)$$

the sensor measurements $y_1(t), y_2(t), \ldots, y_M(t)$ can be represented by only P coefficients $c_1(t), \ldots, c_P(t)$. Since we assume $P < M$, the data dimension is reduced from M to P in equation (19).

The problem here is how to find basis vectors $\boldsymbol{u}_1, \ldots, \boldsymbol{u}_P$ which satisfy the relationship in equation (19). A method of deriving the basis vectors based on the prior knowledge of signal source locations has been proposed in [23]. In this proposed method, the augmented lead field matrix $\bar{\boldsymbol{F}}$ is defined over a local region that just contains the signal sources. The voxels are defined over this local region and the voxel locations are denoted $\bar{\boldsymbol{r}}_1, \ldots, \bar{\boldsymbol{r}}_{\bar{N}}$. The augmented leadfield matrix over these voxel locations is expressed as

$$\bar{\boldsymbol{F}} = \left[\boldsymbol{L}(\bar{\boldsymbol{r}}_1), \ldots, \boldsymbol{L}(\bar{\boldsymbol{r}}_{\bar{N}})\right], \quad (20)$$

and its singular value decomposition is given by

$$\bar{\boldsymbol{F}} = \sum_{j=1}^{R} \bar{\lambda}_j \bar{\boldsymbol{e}}_j \bar{\boldsymbol{f}}_j^T \quad (21)$$

where $R = \min\{M, \bar{N}\}$. Let us assume that the leading $\bar{\tau}$ singular values, $\bar{\lambda}_1, \ldots, \bar{\lambda}_{\bar{\tau}}$ are distinctively large, compared to the rest of the singular values $\bar{\lambda}_{\bar{\tau}+1}, \ldots, \bar{\lambda}_R$. Then, the beamspace basis vectors $\boldsymbol{u}_1, \ldots, \boldsymbol{u}_P$ are obtained as the leading $\bar{\tau}$ singular vectors $\bar{\boldsymbol{e}}_1, \ldots, \bar{\boldsymbol{e}}_{\bar{\tau}}$ where P is equal to $\bar{\tau}$.

3.2. bDSSP algorithm

Use of the beamspace basis vectors with the DSSP algorithm leads to a novel algorithm that can selectively detect signals from a deep source by suppressing interference from superficial sources. The algorithm is called bDSSP, which is described as follows: The data model for the bDSSP algorithm is expressed as

$$\boldsymbol{B} = \boldsymbol{B}_{\text{deep}} + \boldsymbol{B}_{\text{sup}} + \boldsymbol{B}_{\boldsymbol{\varepsilon}}, \quad (22)$$

where $\boldsymbol{B}_{\text{deep}}$ indicates the signal caused from a deep source[7], and $\boldsymbol{B}_{\text{sup}}$ the signal from superficial sources. A prerequisite of this algorithm is that the location of the deep source be

[7]We assume that the target deep source is a single source for simplicity.

known. We then compute the beamspace basis vectors $\boldsymbol{u}_1,\ldots,\boldsymbol{u}_P$ by setting the local source space as a small region just covering the location of the deep source.

The beamspace projector $\boldsymbol{P}_{\text{deep}}$ is then derived as

$$\boldsymbol{P}_{\text{deep}} = [\boldsymbol{u}_1,\ldots,\boldsymbol{u}_P][\boldsymbol{u}_1,\ldots,\boldsymbol{u}_P]^T. \quad (23)$$

By multiplying $\boldsymbol{P}_{\text{deep}}$ and $\boldsymbol{I} - \boldsymbol{P}_{\text{deep}}$ with the data matrix $\boldsymbol{B}$, we obtain:

$$\boldsymbol{P}_{\text{deep}}\boldsymbol{B} = \boldsymbol{B}_{\text{deep}} + \boldsymbol{P}_{\text{deep}}\boldsymbol{B}_{\text{sup}} + \boldsymbol{P}_{\text{deep}}\boldsymbol{B}_{\boldsymbol{\varepsilon}}, \quad (24)$$

$$\left(\boldsymbol{I} - \boldsymbol{P}_{\text{deep}}\right)\boldsymbol{B} = \left(\boldsymbol{I} - \boldsymbol{P}_{\text{deep}}\right)\boldsymbol{B}_{\text{sup}} + \left(\boldsymbol{I} - \boldsymbol{P}_{\text{deep}}\right)\boldsymbol{B}_{\boldsymbol{\varepsilon}}. \quad (25)$$

Here, we use $\boldsymbol{P}_{\text{deep}}\boldsymbol{B}_{\text{deep}} = \boldsymbol{B}_{\text{deep}}$. Then, by using exactly the same derivations as in [27], we can derive

$$\text{rsp}\left(\boldsymbol{P}_{\text{deep}}\boldsymbol{B}\right) \subset \mathcal{K}_{\text{sup}} + \mathcal{K}_{\text{deep}} + \overline{\mathcal{K}}_{\varepsilon}, \quad (26)$$

$$\text{rsp}\left(\left(\boldsymbol{I} - \boldsymbol{P}_{\text{deep}}\right)\boldsymbol{B}\right) \subset \mathcal{K}_{\text{sup}} + \overline{\mathcal{K}}'_{\varepsilon}, \quad (27)$$

where $\mathcal{K}_{\text{deep}}$ and $\mathcal{K}_{\text{sup}}$ are the time-domain signal subspaces of the deep and superficial sources, respectively. We also use the notations: $\text{rsp}\left(\boldsymbol{P}_{\text{deep}}\boldsymbol{B}_{\boldsymbol{\varepsilon}}\right) = \overline{\mathcal{K}}_{\varepsilon}$ and $\text{rsp}\left(\left(\boldsymbol{I} - \boldsymbol{P}_{\text{deep}}\right)\boldsymbol{B}_{\boldsymbol{\varepsilon}}\right) = \overline{\mathcal{K}}'_{\varepsilon}$. Using equations (26) and (27), We can finally derive,

$$\mathcal{K}_{\text{sup}} \supset \text{rsp}\left(\boldsymbol{P}_{\text{deep}}\boldsymbol{B}\right) \cap \text{rsp}\left(\left(\boldsymbol{I} - \boldsymbol{P}_{\text{deep}}\right)\boldsymbol{B}\right). \quad (28)$$

The equation above indicates that the intersection between the row spaces of $\boldsymbol{P}_{\text{deep}}\boldsymbol{B}$ and $(\boldsymbol{I} - \boldsymbol{P}_{\text{deep}})\boldsymbol{B}$ forms a subset of $\mathcal{K}_{\text{sup}}$.

The orthonormal basis set of the intersection, $\text{rsp}(\boldsymbol{P}_{\text{deep}}\boldsymbol{B}) \cap \text{rsp}((\boldsymbol{I} - \boldsymbol{P}_{\text{deep}})\boldsymbol{B})$, can be obtained using the procedure presented in [24, 27, 28]. Denoting these orthonormal basis vectors by $\boldsymbol{\phi}_1,\ldots,\boldsymbol{\phi}_r$, the projector onto the intersection is obtained as

$$\boldsymbol{\Pi}_{isc} = [\phi_1,\ldots,\phi_r][\phi_1,\ldots,\phi_r]^T.$$

Using this $\boldsymbol{\Pi}_{isc}$ as the projector onto the signal subspace $\mathscr{K}_{\text{sup}}$, the signal from the deep source is estimated by projecting the rows of the data matrix onto the direction orthogonal to $\mathscr{K}_{\text{sup}}$, such that

$$\hat{\boldsymbol{B}}_{\text{deep}} = \boldsymbol{B}\left(\boldsymbol{I} - \boldsymbol{\Pi}_{isc}\right) = \boldsymbol{B}\left(\boldsymbol{I} - [\phi_1, \ldots, \phi_r][\phi_1, \ldots, \phi_r]^T\right). \quad (29)$$

Note that since the basis vectors $\boldsymbol{\phi}_1,\ldots, \boldsymbol{\phi}_r$ span only a part of $\mathscr{K}_{\text{sup}}$, the orthogonal projection on the right-hand side of equation (29) cannot perfectly remove $\boldsymbol{B}_{\text{sup}}$. Nonetheless, when $\text{rsp}\left(\boldsymbol{P}_{\text{deep}}\boldsymbol{B}\right) \cap \text{rsp}\left(\left(\boldsymbol{I} - \boldsymbol{P}_{\text{deep}}\right)\boldsymbol{B}\right) \approx \mathscr{K}_{\text{sup}}$ holds, a significant reduction of $\boldsymbol{B}_{\text{sup}}$ can be attained. One such situation is the case in which the superficial signal $\boldsymbol{B}_{\text{sup}}$ is dominated in $\boldsymbol{B}$.

The procedure of the bDSSP algorithm can be summarized as follows:

1. Set the local source space so that it covers the location of the target deep source, and compute the beamspace projector $\boldsymbol{P}_{\text{deep}}$ using equation (23).
2. Apply the projector $\boldsymbol{P}_{\text{deep}}$ to the data matrix $\boldsymbol{B}$ to create two data sets $\boldsymbol{P}_{\text{deep}}\boldsymbol{B}$ and $(\boldsymbol{I} - \boldsymbol{P}_{\text{deep}})\boldsymbol{B}$.
3. Apply the singular value decomposition to $\boldsymbol{P}_{\text{deep}}\boldsymbol{B}$ to derive the orthonormal basis set of $\text{rsp}(\boldsymbol{P}_{\text{deep}}\boldsymbol{B})$; the basis set is denoted by $\{\boldsymbol{x}_1,\ldots,\boldsymbol{x}_\mu\}$ where μ is the dimension of $\text{rsp}(\boldsymbol{P}_{\text{deep}}\boldsymbol{B})$. Also, apply the singular value decomposition to $(\boldsymbol{I} - \boldsymbol{P}_{\text{deep}})\boldsymbol{B}$ to derive the orthonormal basis set of $\text{rsp}((\boldsymbol{I} - \mathbf{P}_{\text{deep}})\boldsymbol{B})$; the basis set is denoted by $\{\mathbf{y}_1,\ldots,\boldsymbol{y}_\nu\}$ where ν is the dimension of $\text{rsp}((\boldsymbol{I} - \mathbf{P}_{\text{deep}})\boldsymbol{B})$.
4. Define matrices $\boldsymbol{X} = \left[\boldsymbol{x}_1^T, \ldots, \boldsymbol{x}_\mu^T\right]$ and $\boldsymbol{Y} = \left[\boldsymbol{y}_1^T, \ldots, \boldsymbol{y}_\nu^T\right]$, and compute the singular value decomposition of $\boldsymbol{X}^T\boldsymbol{Y}$, such that

$$\boldsymbol{X}^T\boldsymbol{Y} = \boldsymbol{Q}\begin{bmatrix}\gamma_1 & \cdots & 0 \\ \vdots & \ddots & \vdots \\ 0 & \cdots & \gamma_\nu\end{bmatrix}\boldsymbol{T}^T, \quad (30)$$

   where $\boldsymbol{Q}$ and $\boldsymbol{T}$ are matrices whose columns consist of the singular vectors.
5. Observe the relation:

$$\gamma_1 = \gamma_2 = \cdots = \gamma_r \approx 1 > \gamma_{r+1} \geqslant \cdots \geqslant \gamma_\nu,$$

   and determine the dimension of the intersection $\text{rsp}(\boldsymbol{P}_{\text{deep}}\boldsymbol{B}) \cap \text{rsp}((\boldsymbol{I} - \boldsymbol{P}_{\text{deep}})\boldsymbol{B})$ to be r.
6. Obtain the orthonormal basis set of the intersection $\text{rsp}(\boldsymbol{P}_{\text{deep}}\boldsymbol{B}) \cap \text{rsp}((\boldsymbol{I} - \boldsymbol{P}_{\text{deep}})\boldsymbol{B})$ as the first r columns of the matrix $\boldsymbol{XQ}$, which are denoted $\boldsymbol{\phi}_1,\ldots, \boldsymbol{\phi}_r$.
7. Estimate the sensor time courses of the deep source by applying equation (29).

8. Apply any of the source localization methods to obtain source images.

4. Computer simulations

A series of computer simulations were carried out to test the effectiveness of our proposed algorithm. A sensor alignment of the 275-channel whole-head sensor array from the Omega (VMS Medtech, Coquitlam, Canada) neuromagnetometer was used. The sensor lead field was computed using the Sarvas formula [25] with the sphere origin set at (0.1, 0, 6.3). In our computer simulation, three sources, (two superficial sources and one deep source), were assumed. The locations of the three sources are shown with sensor locations in figure 1. In this figure, the filled circles indicate the locations of the sensors; the location of the deep source is indicated by the blank circle; and the locations of the two superficial sources are indicated by the square and the triangle. The sphere origin is indicated by a cross mark.

The source properties (the locations, orientations, and distances from the sphere origin) are summarized in table 1. Note that, in our computer simulations, Source#2 is considered the deep source and the other two sources are considered the superficial sources. The distance of Source#2 to the sphere origin was set to 4.4 cm, and distances of the other sources to the sphere origin were set between 6 and 7 cm. The time courses assigned to these three sources are shown in figure 2. The time t is expressed with the unit of time points ranging from $t = -1200$ to 1200. Sensor time courses were generated by projecting the source time courses in figure 2 through the sensor lead field.

We first performed simulations with a moderately high signal-to-interference ratio. Simulated sensor measurements were computed by adding the sensor time courses generated from the deep source and those from the superficial source. We set the ratio $\gamma = \|\boldsymbol{B}_{\text{deep}}\|_{\text{F}}/\|\boldsymbol{B}_{\text{sup}}\|_{\text{F}}$ to be one at which $\|\boldsymbol{X}\|_{\text{F}}$ indicates the Frobenius norm of a matrix $\boldsymbol{X}$[8]. This ratio γ is called the signal to interference ratio (SIR), because, in our experiments, the magnetic field from the superficial sources is considered the interference, and that from the deep source considered the signal. The simulated sensor measurements given by $\boldsymbol{B} = \boldsymbol{B}_{\text{deep}} + \boldsymbol{B}_{\text{sup}} + \boldsymbol{B}_{\boldsymbol{e}}$ are shown in the top panel of figure 3(a). Here, a moderare amount of white Gaussian noise was added to simulate the sensor noise and the SNR defined as $\|\boldsymbol{B}_{\text{deep}}\|_{\text{F}}/\|\boldsymbol{B}_{\boldsymbol{e}}\|_{\text{F}}$ was set at 4.5. The middle panel of figure 3(a) shows $\boldsymbol{B}_{\text{deep}} + \boldsymbol{B}_{\boldsymbol{e}}$, which are the sensor time courses generated from only the deep source with the same amount of the sensor noise added. These time courses work as the ground truth for our experiments described below.

We applied the proposed bDSSP algorithm to the simulated measurements shown in the top panel, and the results are shown in the bottom panel of figure 3(a). In the application, the local source space was chosen as a 2 cm cubic region whose center was equal to the location of the deep source. The results show that by using the bDSSP algorithm, time courses nearly identical to those of the ground truth (in the middle panel) were obtained. These results show that the bDSSP algorithm effectively suppresses the interference from the superficial source and the signal sensor time courses from the deep-source can be retrieved.

[8] As defined in equation (22), $\boldsymbol{B}_{\text{sup}}$ and $\boldsymbol{B}_{\text{deep}}$ are the signal matrices corresponding to superficial and deep sources.

In our computer simulations, the correlation between the groun truth (the sensor time courses $\boldsymbol{B}_{\text{deep}} + \boldsymbol{B}_{\boldsymbol{\varepsilon}}$ in the middle panel of figure 3(a)) and the bDSSP-processed sensor time courses $\hat{\boldsymbol{B}}_{\text{deep}}$ (in the bottom panel of figure 3(a)) is computed such that

$$\Phi = \frac{1}{M} \sum_{m=1}^{M} \rho_m, \quad (31)$$

where ρ_m is the correlation coefficient between the mth row of $\hat{\boldsymbol{B}}_{\text{deep}}$ and that of $\boldsymbol{B}_{\text{deep}} + \boldsymbol{B}_{\boldsymbol{\varepsilon}}$. Here, Φ is computed by averaging ρ_m across all sensor channels. This Φ can be a measure indicating how well the bDSSP algorithm can retrieve the sensor time courses from the target deep source, and is called the sensor time-course correlation. The results in the bottom of figure 3(a) attain Φ of 0.85. We use this Φ to assess the results in our Monte Carlo experiments below.

We next conducted computer simulations for a case of significantly low SIR of 0.05. That is, the interference from superficial sources was 20 times stronger than the signal from the deep source. The generated sensor time courses in this case are shown in the top panel of figure 3(b). The results of applying the bDSSP algorithm are shown in the bottom panel. The results here also attain Φ of 0.85, and this fact indicates that the proposed bDSSP algorithm still effectively removed the interference from the superficial sources even when SIR was so low.

We performed source reconstruction experiments using these simulated sensor data with SIR of 0.05. The adaptive beamformer reconstruction algorithm [22] was applied to the data in figures 3(b). The results of the reconstruction experiments are shown in figure 4. In these experiments, voxels were defined with 0.5 cm interval. The locations of the three sources were set at one of voxel locations. In these results in figure 4, the sources were reconstructed exactly at their assumed locations.

The source image from the simulated sensor measurements in the top panel of figure 3(b) is shown in figure 4(a). Here, the top left, top right and bottom panels, respectively, show the axial, coronal and sagittal projections of the 3D source distribution. In these results, two superficial sources are reconstructed, but the deep source was not clearly reconstructed because of a large intensity difference between the superficial and deep sources. Note that the cross marks in figure 4(a) indicate the location of the deep source. The source reconstruction results obtained using the bDSSP-processed sensor data in the bottom panel of figure 3(b) are shown in figure 4(b). Here, the target deep source is successfully reconstructed, demonstrating the effectiveness of the proposed algorithm.

We also performed source reconstruction experiments using low SIR and low SNR data, in order to see the effect of the sensor noise on the algorithm performance. The same computer simulation as for the low SIR experiments mentioned above was used. However, in this case, the sensor noise was added such that the SNR (defined as $\|\boldsymbol{B}_{\text{deep}}\|_F / \|\boldsymbol{B}_{\boldsymbol{\varepsilon}}\|_F$) was approximately equal to 1.5. The bDSSP-processed sensor time courses are shown in figure

5(a). These results show that the sensor time courses of the deep-source still can be retrieved. The results of source reconstruction obtained from these sensor data are shown in figure 5(b). Again, the deep source is clearly reconstructed, although these results have a small localization error of 0.7 cm, which was obtained as the distance between the assumed and reconstructed locations of the deep source[9].

In computer simulations so far, the local source space was chosen as a 2 cm cubic region whose center was exactly equal to the location of the deep source. However, in real-life applications, the estimated location of the target deep source may have some uncertainty. Therefore, we conducted Monte Carlo computer simulation to see the robustness of the bDSSP algorithm to the mismatch between the position of the local source space and the location of the target deep source. In this simulation, the distance between the deep source and the center of the local source space was set at several non-zero values, keeping the local source space to be the same 2 cm cubic volume. This distance is called the mismatch distance and denoted by D. Here, to assess the algorithm performance, we used two measures: the sensor time-course correlation Φ in equation (31) and the localization error of the deep source.

Results of the experiments are shown in figure 6. Here, the top panel shows the plots of the sensor-time course correlation Φ versus the mismatch distance D. The bottom panel indicates the plots of the localization error of the deep source versus D. In these Monte Carlo experiments, at each value of D, the position of the local source space was set to fifty random locations having the same D. In the plots in figure 6, a filled dot indicates the results of each Monte Carlo trial, and a blank circle indicates the average across the results at each value of D. These plots show that when D is less than 1 cm, there is nearly no influence and even when $D = 1.5$ cm, the influence is still very small, demonstrating the algorithm's robustness to the mismatch between the local source space and the target source location.

Finally, we conducted Monte Carlo simulation to see the robustness of the bDSSP algorithm to the source configuration. In this simulation, one hundred Monte Carlo trials were generated, and in each trial, the location and orientation of the deep source were randomly chosen. One hundred locations of the deep source generated in this Monte Carlo study are shown by cross marks in figure 7(a). In this study, a random value between 0 and 1 cm was assigned to the mismatch distance D. The results of these one hundred Monte Carlo trials were assessed by using the sensor time course correlation Φ and the source localization error.

In figure 7(b), the histogram of Φ is shown at the top panel, and the histogram of source localization errors is shown at the bottom panel. Here, SNR was set equal to 4.5 and SIR (γ) equal to 0.05. In these results, the 96% of the Monte Carlo trials attain the values of Φ between 0.8 and 0.9. Also, 97% of the Monte Carlo results attain the localization errors less than 0.8 cm. Note that, in this Monte Carlo study, since the deep source location was randomly chosen, the source was not necessarily located at one of voxel locations, and the localization error also contains contributions from the voxel discretization, which is 0.25 cm

[9]The reconstructed source location was defined as the location of the peak maximum.

in average for this study that uses the voxel interval of 0.5 cm. The results of these Monte Carlo experiments demonstrate that the performance of the bDSSP algorithm is not much affected by the configuration of the deep source with respect to superficial sources.

5. Experiments

5.1. Experiments using phantom data

5.1.1. Phantom data measurements.—Experiments using data from an MEG phantom were performed to test the usefulness of the proposed algorithm. The phantom used in our experiments is shown in figure 8. In this phantom, dipole sources consist of isosceles-triangular-shaped coils; these triangular coils generate magnetic fields expressed by the Sarvas formula [25]. Thus, the coils behave like dipole sources in the spherical homogeneous conductor [29]. A phantom using such triangular coils is called a dry phantom [30]. The triangular coils installed on the surface of a disc-shaped phantom can be seen in figures 8(a) and (b), in which the squares with a pale color show the locations of the coils. The center of the disc matches the sphere origin of the spherical conductor.

A whole-head MEG system with a 160-channel sensor array [31], installed at Applied Electronics Laboratory, Kanazawa Institute of Technology, Amaike, Kanazawa, Japan, was used to measure the phantom data. Figure 8(c) shows how the phantom was installed within the bore of the MEG sensor helmet. The phantom is equipped with marker coils, which were used to match between the phantom and sensor coordinates.

5.1.2. Experiments using dipole pair#1.—We performed two cases of experiments using different dipole pairs. The first case used a pair of dipole sources shown with the annotation ‘Dipole pair#1’ in figure 8(a). These dipoles are perpendicular to each other and 2 cm apart. The pair was placed near the parietal-lobe region. The superficial dipole, which is annotated as ‘4–1’, was driven by an 11 Hz sinusoid with a current strength of 1.42 mA. The deep dipole, annotated as ‘4–2’, was driven by an amplitude-modulated sinusoid in which the carrier frequency was 15 Hz and the modulation frequency was 1 Hz. The current strength to drive the deep dipole was 0.225 mA. The current values of the two dipoles were chosen in order for the magnetic field of the superficial dipole to have a 16-times stronger intensity than that of the deep dipole. Namely, the signal-to-interference ratio (SIR), γ, was set to 1/16 in the first experiments. The data were acquired for 2 s using a sampling frequency of 1 kHz.

The 160-sensor time courses measured when only the superficial dipole was active are shown in figure 9(a), and the time courses measured when only the deep dipole was active are shown in figure 9(b). Adaptive beamformer source reconstruction was applied to these data sets. The image of the superficial dipole is shown in figure 9(c), and the image of the deep dipole is shown in figure 9(d). The sensor time courses and the dipole location of the deep source in figures 9(b) and (d) work as the ground truth in the following experiments.

The 160-sensor time courses measured when the superficial and deep dipoles were simultaneously active are shown in figure 10(a). In these sensor data, since the signal from the superficial dipole was sixteen times stronger than the signal from the deep dipole, the

sensor time courses were dominated by the signal from the superficial source. Source reconstruction results from these sensor data are shown in figure 10(c). Although the sensor data only show the dominated superficial dipole activity, the reconstruction results show both the superficial and deep dipoles.

We then applied the bDSSP algorithm to detect the signal from the deep source. We set the local source space at a 1 cm-cubic region whose center was equal to the location of the deep dipole. The bDSSP algorithm was applied to the sensor data in figure 10(a) to extract the signal from the deep source. The resultant sensor time courses are shown in figure 10(b), and source reconstruction results are shown in figure 10(d). Comparisons between these results and those in figures 9(b) and (d) demonstrate that the proposed bDSSP algorithm can successfully extract the activity of the deep dipole from the sensor data dominated by a large interference from the superficial source. Note that the difference between the source locations in figures 9(d) and 10(d) is 0.5 cm.

5.1.3. Experiments using dipole pair#2.—We conducted the same experiments using a pair of dipole sources shown with the annotation ‘Dipole pair#2’ in figure 8(a). These dipoles are parallel to each other and 4 cm apart, and they were placed near the temporal-lobe region. The superficial dipole, which is annotated as ‘2–1’, was driven by an 11 Hz sinusoid with a current strength of 0.71 mA. The deep dipole, annotated as ‘1–2’, was driven with the same amplitude-modulated sinusoid as in the previous experiments with a current strength of 0.5 mA. These current values were chosen in order for the intensity of the magnetic field from the superficial dipole to be eight times stronger than that from the deep dipole. The reconstruction results of the superficial dipole are shown in figure 11(a). The reconstruction results of the deep dipole are shown in figure 11(b).

The sensor time courses obtained when the superficial and deep dipoles were simultaneously active are shown in figure 12(a). Again, the sensor data were dominated by the signal from the superficial dipole. Results of source reconstruction applied to these sensor data are shown in figure 12(c). In these results, since the superficial source is dominated, the deep dipole can hardly be seen. We applied the bDSSP algorithm for the removal of the interference from the superficial source activity. The resultant sensor time courses are shown in figure 12(b). These results show that the interference signal from the superficial dipole was successfully removed. The source reconstruction results obtained using these bDSSP-processed sensor data are shown in figure 12(d). Although considerable blur was introduced and the difference between the source locations in figures 11(b) and 12(d) is 2.5 cm in this case, the deep dipole can still be detected in figure 12(d).

In figure 12(d), the resultant source image contains a large blur and a fairly large localization error was caused. This is due to the high spatial correlation between the lead fields of the two sources [22]. (Since the two sources are parallel dipoles, the similarity of their lead fields are considerably high, even though they are 4 cm apart.) By making use of the blur in the bDSSP results, we can make a rough estimate on how much signal from the superficial source remains in the bDSSP-processed results. Let us denote the sensor data measured when only the superficial dipole (dipole’2–1’) was active by $\boldsymbol{y}_{\text{sup}}(t)$, and the data measured when only the deep dipole (dipole ‘1–2’) was active by $\boldsymbol{y}_{\text{deep}}(t)$. Then, the synthetic sensor

data $\boldsymbol{y}_{sy}(t)$ is computed such that $\boldsymbol{y}_{sy}(t) = \boldsymbol{y}_{deep}(t) + \alpha \boldsymbol{y}_{sup}(t)$ where the positive value α controlled the mixture ratio. The source reconstruction results using $\boldsymbol{y}_{sy}(t)$ with $\alpha = 0.04$, $\alpha = 0.02$, and $\alpha = 0.01$ are shown in figures 13(a)–(c), respectively.

Let us compare these reconstruction results with the bDSSP interference removal results in figure 12(d), and we can see that the results in figure 13(b) are closest to those in figure 12(d), This observation leads to the estimation that the value of α could be around 0.02 in the bDSSP results in figure 12(d). Since the value of α was equal to 8 in the original sensor data shown in figure 12(a), the attenuation of the interference signal from the superficial dipole is estimated as 0.02/8 = 1/400. That is, we can estimate that the bDSSP algorithm has reduced the intensity of the superficial interference by a factor of 400 in this experiment.

5.2. Experiments using real MEG data

The bDSSP algorithm was also applied to somatosensory MEG data to further demonstrate its usefulness. The data set was collected from a healthy subject using the 275-channel CTF MEG scanner. Vibrotactile stimuli were applied to a subject's right index finger for a total of 240 trials, and sensor time courses were averaged across these trials time-aligned to the onset of the tactile stimulus. The averaged sensor time courses are shown in the upper panel in figure 14(a) in which a peak due to the activity from the hand area in the primary somatosensory cortex (S1) can be seen 50–60 ms after stimulation. The results of source reconstruction from these sensor data are shown in the upper panel of figure 14(b). Here, we used the sparse Bayesian (Champagne) source reconstruction algorithm developed by our group [32, 33]. In these results, a clear and focussed activity (labelled as (A)) arising from the primary somatosensory cortex can be observed. However, no other somatosensory activities that are weaker than the activity in the primary somatosensory cortex were detected.

We applied the bDSSP algorithm in order to detect weaker somatosensory cortical activity by suppressing the strong S1 activity. A local source space was set so that it covers more ventral regions of the somatosensory cortex, as indicated by the rectangles in figure 14(b). The sensor time courses of the bDSSP results are shown in the bottom panel of figure 14(a). Here, it can be seen that the large peak near 50 ms is removed. The results of source reconstruction obtained from these time courses are shown in the bottom panel of figure 14(b). Here, three sources, not observed in the original reconstruction image (in the upper panel of figure 14(b)), can be observed. (They are labelled as (B)–(D).)

The reconstructed source time courses are shown in figure 14(c). These time courses indicate that the three sources observed in the results in the bottom panel of figure 14(b) were stimulus elicited. The results in the bottom panel of figure 14(b) show that the two sources labeled as (B) and (D) are located on the posterior bank of the central sulcus and considered as somatosensory activities. The third source, labeled as (C), is located near the supplementary motor area (SMA) and can also be considered as a somatosensory-related activity. These results demonstrate the usefulness of the bDSSP algorithm for investigating weak brain activities usually hidden by simultaneously-existing, much stronger activities.

6. Complementary bDSSP algorithm

There can be a complementary way to implement the bDSSP algorithm. In the complementary version, the prerequisite of the algorithm is the information on the location of the superficial (interference) sources. The local source space is set at a region including the superficial sources, and beamspace basis vectors are computed by following exactly the same procedure described in section 3. Denoting the basis vectors as $\tilde{\boldsymbol{u}}_1, \ldots, \tilde{\boldsymbol{u}}_P$, we can compute the beamspace projector $\boldsymbol{P}_{\text{sup}}$: $\boldsymbol{P}_{\text{sup}} = [\tilde{\boldsymbol{u}}_1, \ldots, \tilde{\boldsymbol{u}}_P][\tilde{\boldsymbol{u}}_1, \ldots, \tilde{\boldsymbol{u}}_P]^T$. Note that $\boldsymbol{P}_{\text{sup}}$ is a projector onto the pseudo-signal subspace of the superficial source. (In the original bDSSP algorithm, the beamspace projector is denoted $\boldsymbol{P}_{\text{deep}}$ because it is a projector onto the pseudo signal subspace of the deep source.)

By multiplying $\boldsymbol{P}_{\text{sup}}$ and $\boldsymbol{I} - \boldsymbol{P}_{\text{sup}}$ with the data matrix $\boldsymbol{B}$, we obtain

$$\boldsymbol{P}_{\text{sup}}\boldsymbol{B} = \boldsymbol{B}_{\text{sup}} + \boldsymbol{P}_{\text{sup}}\boldsymbol{B}_{\text{deep}} + \boldsymbol{P}_{\text{sup}}\boldsymbol{B}_{\boldsymbol{\varepsilon}}, \quad (32)$$

$$\left(\boldsymbol{I} - \boldsymbol{P}_{\text{sup}}\right)\boldsymbol{B} = \left(\boldsymbol{I} - \boldsymbol{P}_{\text{sup}}\right)\boldsymbol{B}_{\text{deep}} + \left(\boldsymbol{I} - \boldsymbol{P}_{\text{sup}}\right)\boldsymbol{B}_{\boldsymbol{\varepsilon}}, \quad (33)$$

where we use

$$\left(\boldsymbol{I} - \boldsymbol{P}_{\text{sup}}\right)\boldsymbol{B}_{\text{sup}} = 0. \quad (34)$$

Therefore, we can finally derive [27],

$$\mathcal{K}_{\text{deep}} \supset \text{rsp}\left(\boldsymbol{P}_{\text{sup}}\boldsymbol{B}\right) \cap \text{rsp}\left(\left(\boldsymbol{I} - \boldsymbol{P}_{\text{sup}}\right)\boldsymbol{B}\right). \quad (35)$$

The equation above indicates that the intersection, $\text{rsp}(\boldsymbol{P}_{\text{sup}}\boldsymbol{B}) \cap \text{rsp}((\boldsymbol{I} - \boldsymbol{P}_{\text{sup}})\boldsymbol{B})$, forms a subset of $\mathcal{K}_{\text{deep}}$, and the projector onto the intersection, $\boldsymbol{\Pi}_{isc}$, can be used as the projector onto $\mathcal{K}_{\text{deep}}$. Thus, the signal from the deep source is extracted by using $\hat{\boldsymbol{B}}_{\text{deep}} = \boldsymbol{B}\boldsymbol{\Pi}_{isc}$. The algorithm is called the ‘complementary bDSSP’, (cbDSSP) algorithm.

We applied the cbDSSP algorithm to the computer-generated data in the top panel of figure 3(a), and the results are shown in figure 15(a). The algorithm effectively removed the interference in this computer simulation. We then applied the cbDSSP algorithm to the phantom data in figure 10(a) obtained using dipole pair#1, and the results are shown in figure 15(b). Here, the algorithm fails to remove the interference from the superficial dipole.

Figure 15(c) shows $\boldsymbol{P}_{\text{sup}}\boldsymbol{B}$ and $(\boldsymbol{I} - \boldsymbol{P}_{\text{sup}})\boldsymbol{B}$ in these phantom experiments. The data set $\boldsymbol{P}_{\text{sup}}\boldsymbol{B}$ is shown in the upper panel and $(\boldsymbol{I} - \boldsymbol{P}_{\text{sup}})\boldsymbol{B}$, in the lower panel. Here, the two data sets are normalized by the same value, (the maximum value of $\boldsymbol{P}_{\text{sup}}\boldsymbol{B}$). It can be seen in figure 15(c)

that although most of $\boldsymbol{B}_{\text{sup}}$ components were removed in $(\boldsymbol{I} - \boldsymbol{P}_{\text{sup}})\boldsymbol{B}$, a small amount of 11 Hz sinusoid, the component from the superficial source, still remains. This is probably because $\boldsymbol{B}_{\text{sup}}$ is much stronger than $\boldsymbol{B}_{\text{deep}}$ in the phantom data in figure 10(a)[10].

The failure of the cbDSSP algorithm in the phantom experiments indicates one of its limitations. While the bDSSP algorithm uses the projector $\boldsymbol{P}_{\text{deep}}$ to suppress the signal from the deep source, the cbDSSP algorithm uses $\boldsymbol{P}_{\text{sup}}$ to suppress the signal from the superficial source. Since it is generally true that the signal from the superficial source is much stronger than the signal from the deep source, the cbDSSP algorithm must be less robust to various types of errors. This is because such errors may force $(\boldsymbol{I} - \boldsymbol{P}_{\text{sup}})\boldsymbol{B}_{\text{sup}}$ to have non-zero values, while $(\boldsymbol{I} - \boldsymbol{P}_{\text{deep}})\boldsymbol{B}_{\text{deep}}$ approximates zero.

7. Discussion and summary

The beamspace SSS method [14] has been proposed to attain the selective detection of components from deep sources by suppressing components from superficial sources. In the original SSS method, signal components of the data vector $\boldsymbol{y}_{\text{S}}$are estimated using the expansion:

$$\hat{\boldsymbol{y}}_{\text{S}}(t) = \sum_{\ell=1}^{\infty} \sum_{m=-\ell}^{\ell} \alpha_{\ell,m} \boldsymbol{c}_{\ell,m}, \quad (36)$$

where $\boldsymbol{c}_{\ell m}$ are the SSS basis vectors for the internal part and $\alpha_{\ell m}$, are called the multipole components, and represent the coefficients of the expansion [15, 16]. Here, the time notation is omitted from $\alpha_{\ell m}$ for simplicity. The beamspace SSS method utilizes the fact that components from superficial sources are represented more by larger ℓterms, and components from deep sources are represented more by smaller ℓterms. Thus, estimating the data vector using only lower-order SSS basis vectors provides an estimated data vector containing more deep-source components and less superficial-source components. This can be achieved in simplest form by truncating the basis vector expansion, as suggested in [14]. That is, to estimate the deep source activity, the beamspace SSS algorithm uses

$$\hat{\boldsymbol{y}}_{\text{deep}}(t) = \sum_{\ell=1}^{L_T} \sum_{m=-\ell}^{\ell} \alpha_{\ell,m} \boldsymbol{c}_{\ell,m}, \quad (37)$$

where $\hat{\boldsymbol{y}}_{\text{deep}}(t)$ is the estimated deep source activity. In the equation above, the summation with respect to the index $\ell$is truncated at L_T. We applied the beamspace SSS algorithm to the simulated sensor data in the top panel of figure 3(a). The results obtained by truncating $\ell$to 1, 2, and 3 are shown in figure 16. The results show that the beamspace SSS can enhance the signal from the deep source. However, considerable amount of signal from the superficial source still remains even when $\ell$is set at 1, the minimum value of ℓThese results suggest

[10]As mentioned, $\boldsymbol{B}_{\text{sup}}$ is sixteen times stronger than $\boldsymbol{B}_{\text{deep}}$ in these phantom data.

that the beamspace SSS method has only a limited capability of suppressing superficial interference.

In our computer simulation and our experiments using phantom data, the spherical homogeneous conductor model was used. One limitation with this conductor model is that the discrepancy between the actual and computed lead fields becomes large for midbrain and deep brain regions. This may affect the performance of the beamspace projector $\boldsymbol{P}_{\text{deep}}$ defined in equation (23). That is, one key factor for the success of the algorithm is that the relationship $(\boldsymbol{I} - \boldsymbol{P}_{\text{deep}})\boldsymbol{B}_{\text{deep}} \approx \boldsymbol{0}$ holds. However, due to the inaccuracy of the conductor model, $(\boldsymbol{I} - \boldsymbol{P}_{\text{deep}})\boldsymbol{B}_{\text{deep}}$ could have non-zero components, which may cause removal of the signal magnetic field from a deep source, as well as removal of the interference from superficial sources. Therefore, to avoid such signal cancellation, a better conductor model, such as the realistic head model, may have to be used with the bDSSP algorithm. We will investigate on this point, and publish the results in a future occasion.

This paper proposes a novel algorithm for selective detection of a deep source by suppressing interference signals from superficial sources in MEG measurements. The proposed algorithm combines the beamspace preprocessing method with the dual signal space projection (DSSP) interference suppression algorithm. A prerequisite of the proposed algorithm is prior knowledge on the location of the deep source. After presenting a concise review on the DSSP interference removal algorithm, this paper introduces a method we call the beamspace DSSP algorithm. Compared with the previously proposed beamspace signal space separation (SSS) method, the proposed algorithm is capable of suppressing much stronger interference from superficial sources. This capability is demonstrated in our computer simulations as well as experiments using phantom data.

The proposed bDSSP algorithm can be a powerful tool in neuroscience studies of physiological functions of midbrain structures such as the thalamus, amygdala, hippocampus and the basal ganglia, and of the cerebellum, because there are many studies that require accurate localization of physiological and pathophysiological activities in deep brain regions. One example is non-invasive imaging studies of neural oscillations that examine the computational role of these brain regions. Other examples include studies on pathophysiological activities from deep brain structures. Such pathologic activities are implicated in a variety of conditions such as epilepsy and dementias (hippocampus and medial temporal lobe), movement disorders (basal ganglia, cerebellum), and neurodevelopmental disorders (thalamus etc). Accurate reconstruction of such activities in deep brain regions can lead to better understanding of these pathological conditions and potentially contributes to improved clinical managements and treatment strategies.

References

[1]. Hämäläinen M, Hari R, Ilmoniemi RJ, Knuutila J and Lounasmaa OV 1993 Magnetoencephalography-theory, instrumentation, and applications to noninvasive studies of the working human brain Rev. Mod. Phys 65 413–97

[2]. Hari R and Salmelin R 2012 Magnetoencephalography: from SQUIDs to neuroscience: neuroimage 20th anniversary special edition Neuroimage 61 386–96 [PubMed: 22166794]

[3]. Supek S and Aine CJ 2016 Magnetoencephalography (Berlin:Springer)

[4]. Attal Y, Bhattacharjee M, Yelnik J, Cottereau B, Lefevre J, Okada Y, Bardinet E, Chupin M and Baillet S 2007 Modeling and detecting deep brain activity with MEG & EEG 29th Annual Int. Conf. of the IEEE Engineering in Medicine and Biology Society (IEEE) pp 4937–40

[5]. Jerbi K et al. 2007 Coherent neural representation of hand speed in humans revealed by MEG imaging Proc. Natl Acad. Sci 104 7676–81 [PubMed: 17442753]

[6]. Tesche C 1996 Non-invasive imaging of neuronal population dynamics in human thalamus Brain Res 729 253–8 [PubMed: 8876995]

[7]. Roux F, Wibral M, Singer W, Aru J and Uhlhaas PJ 2013 The phase of thalamic alpha activity modulates cortical gamma- band activity: evidence from resting-state MEG recordings J. Neurosci 33 17827–35 [PubMed: 24198372]

[8]. Lithari C, Moratti S and Weisz N 2015 Thalamocortical interactions underlying visual fear conditioning in humans Human Brain Mapp 36 4592–603

[9]. Jha A et al. 2016 Functional connectivity of the pedunculopontine nucleus and surrounding region in parkinson's disease Cerebral Cortex 27 54–67 [PubMed: 28316456]

[10]. Luo Q, Holroyd T, Mitchell D, Yu H, Cheng X, Hodgkinson C, Chen G, McCaffrey D, Goldman D and Blair RJ 2017 Heightened amygdala responsiveness in s-carriers of 5-httlpr genetic polymorphism reflects enhanced cortical rather than subcortical inputs: an MEG study Human Brain Mapp 38 4313–21

[11]. Garvert MM, Friston KJ, Dolan RJ and Garrido MI 2014 Subcortical amygdala pathways enable rapid face processing Neuroimage 102 309–16 [PubMed: 25108179]

[12]. Hashimoto I, Kimura T, Tanosaki M, Iguchi Y and Sekihara K 2003 Muscle afferent inputs from the hand activate human cerebellum sequentially through parallel and climbing fiber systems Clin. Neurophysiol 114 2107–17 [PubMed: 14580608]

[13]. Herrojo Ruiz M, Maess B, Altenmuller E, Curio G and Nikulin VV 2017 Cingulate and cerebellar beta oscillations are engaged in the acquisition of auditory-motor sequences Human Brain Mapp 38 5161–79

[14]. Özkurt TE, Sun M and Sclabassi RJ 2008 Decomposition of magnetoencephalographic data into components corresponding to deep and superficial sources IEEE Trans. Biomed. Eng 55 1716–27 [PubMed: 18714836]

[15]. Taulu S and Kajola M 2005 Presentation of electromagnetic multichannel data: the signal space separation method J. Appl. Phys 97 124905

[16]. Taulu S, Simola J and Kajola M 2005 Applications of the signal space separation method IEEE Trans. Signal Process 53 3359–72

[17]. Buckley KM and Xu X-L 1990 Spatial-spectrum estimation in a location sector IEEE Trans. Acoust. Speech Signal Process 38 1842–52

[18]. Lee HB and Wengrovitz MS 1990 Resolution threshold of beamspace MUSIC for two closely spaced emitters IEEE Trans. Acoust. Speech Signal Process 38 1545–59

[19]. Schmidt RO, A signal subspace approach to multiple emitter location and spectral estimation. Stanford University; Stanford, CA: 1981. PhD Thesis

[20]. Mosher JC, Lewis PS and Leahy RM 1992 Multiple dipole modeling and localization from spatio-temporal MEG data IEEE Trans. Biomed. Eng 39 541–57 [PubMed: 1601435]

[21]. Van Veen BD, Van Drongelen W, Yuchtman M and Suzuki A 1997 Localization of brain electrical activity via linearly constrained minimum variance spatial filtering IEEE Trans. Biomed. Eng 44 867–80 [PubMed: 9282479]

[22]. Sekihara K and Nagarajan SS 2008 Adaptive Spatial Filters for Electromagnetic Brain Imaging (Berlin: Springer)

[23]. Rodnguez-Rivera A, Baryshnikov BV, Van Veen BD and Wakai RT 2006 MEG and EEG source localization in beamspace IEEE Trans. Biomed. Eng 53 430–41 [PubMed: 16532769]

[24]. Sekihara K, Kawabata Y, Ushio S, Sumiya S, Kawabata S, Adachi Y and Nagarajan SS 2016 Dual signal subspace projection (DSSP): a novel algorithm for removing large interference in biomagnetic measurements J. Neural Eng 13 036007 [PubMed: 27064933]

[25]. Sarvas J 1987 Basic mathematical and electromagnetic concepts of the biomagnetic inverse problem Phys. Med. Biol 32 11–22 [PubMed: 3823129]

[26]. Ipsen IC 2009 Numerical Matrix Analysis: Linear Systems and Least Squares (Philadelphia: SIAM)

[27]. Sekihara K and Nagarajan SS 2017 Subspace-based interference removal methods for a multichannel biomagnetic sensor array J. Neural Eng 14 051001 [PubMed: 28820740]

[28]. Golub GH and Van Loan CF 2012 Matrix Computations vol 3 (Baltimore, MD: Johns Hopkins University Press)

[29]. Ilmoniemi R, Hämäläinen M and Knuutila J 1985 The forward and inverse problems in the spherical model Biomagnetism: Applications and Theory ed Weinberg H et al. (Oxford: Pergamon)

[30]. Oyama D, Adachi Y, Yumoto M, Hashimoto I and Uehara G 2015 Dry phantom for magnetoencephalography: configuration, calibration, and contribution J. Neurosci. Methods 251 24–36 [PubMed: 25985908]

[31]. Uehara G, Adachi Y, Kawai J, Shimogawara M, Higuchi M, Haruta Y, Ogata H and Hisashi K 2003 Multi-channel SQUID systems for biomagnetic measurement IEICE Trans. Electron 86 43–54

[32]. Wipf DP, Owen JP, Attias HT, Sekihara K and Nagarajan SS 2010 Robust Bayesian estimation of the location, orientation, and time course of multiple correlated neural sources using MEG NeuroImage 49 641–55 [PubMed: 19596072]

[33]. Sekihara K and Nagarajan SS 2015 Electromagnetic Brain Imaging: a Bayesian Perspective (Berlin: Springer)

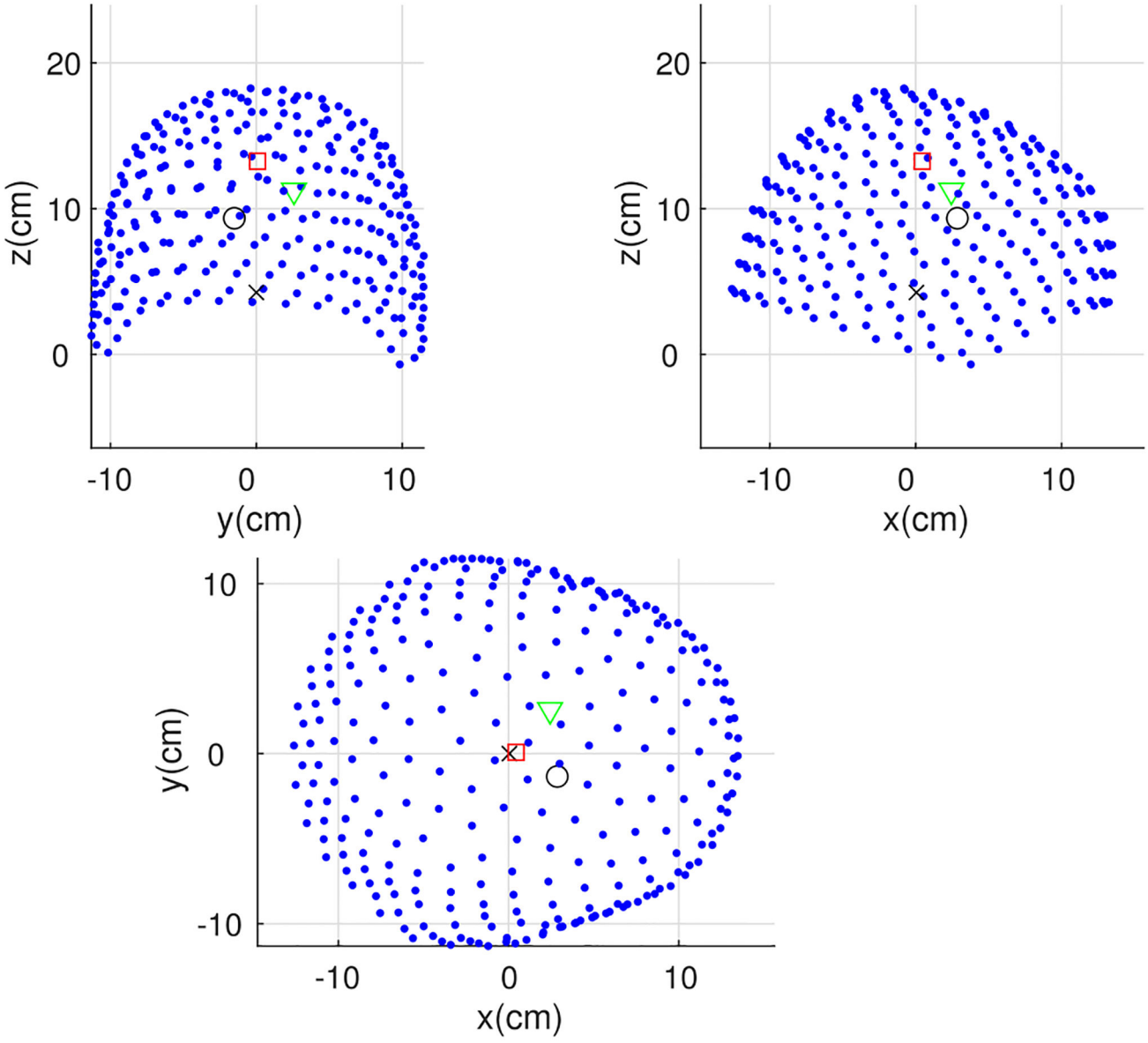

Figure 1.

Locations of sensors and three sources assumed in our computer simulations. Filled circles indicate the locations of sensors, the blank circle indicates the location of the deep source, and the square and triangle indicate the locations of the two superficial sources. The cross mark indicates the sphere origin. Top-left, top-right, and bottom panels, respectively, show the coronal, sagittal, and axial projections. The source locations, orientations and distances to the sphere origin are shown in table 1 in which Source#2 is the deep source, and the other two sources are called the superficial sources in our computer simulations.

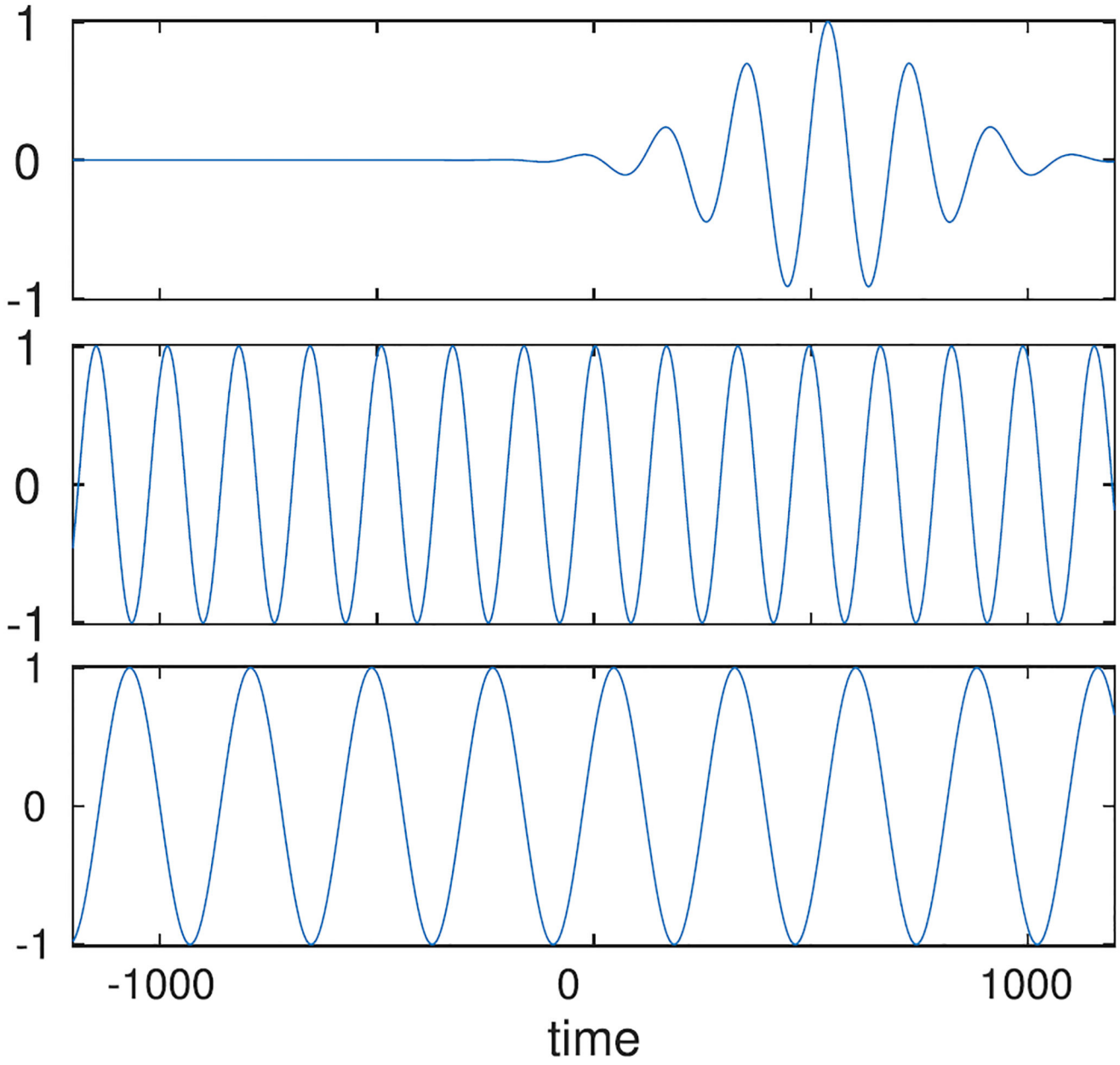

Figure 2.

Time courses assigned to the three sources. Time t is expressed with the unit of time points. Top panel shows the time course assigned to the deep source, and the bottom two panels show the time courses assigned to the two superficial sources. Each time course is normalized between − 1 and 1.

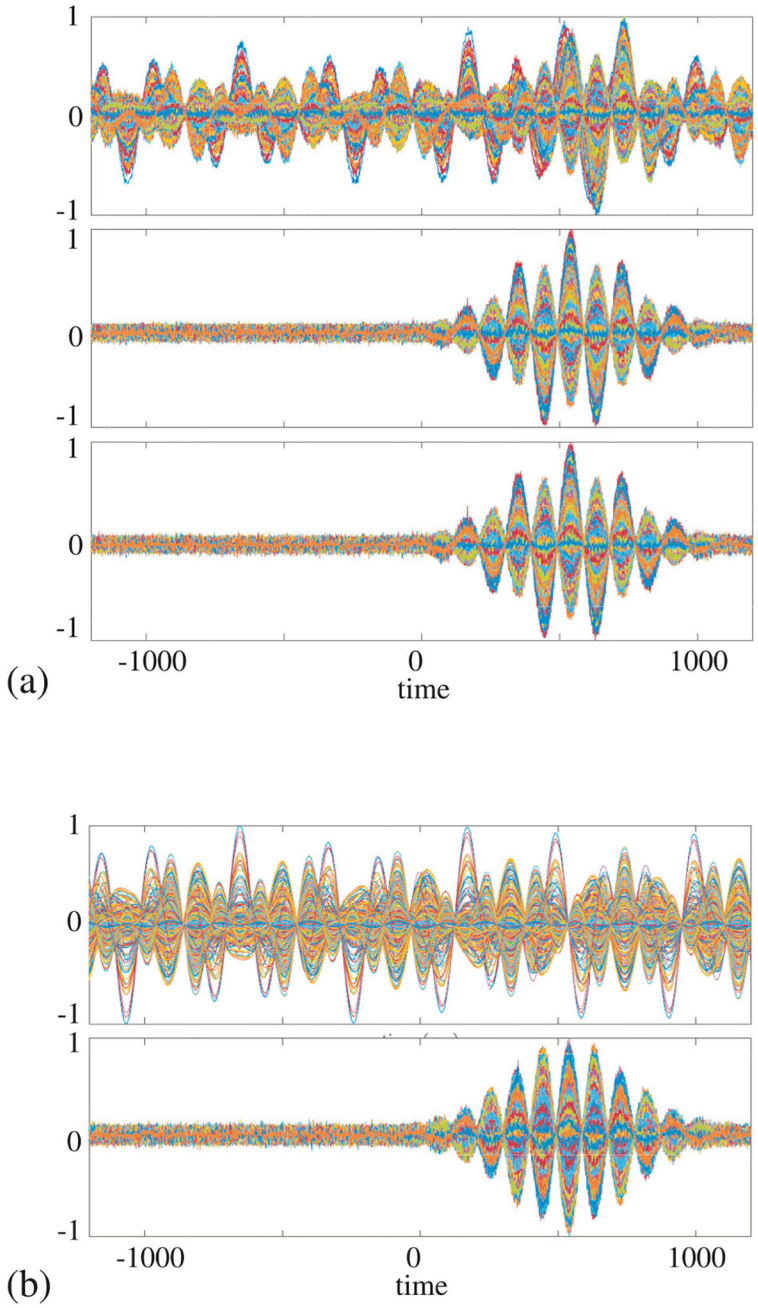

Figure 3.

(a) Results of experiments when the signal to interference ratio (SIR), γ, was set to one. Top panel: simulated sensor time courses generated when one deep and two superficial sources are active. Middle panel: sensor time courses generated when only the deep source is active with the same amount of the sensor noise added. Bottom panel: results of applying the bDSSP algorithm to the sensor data in the top panel. (b) Results of the same experiments except that SIR (γ) was set to 0.05. Top panel: simulated sensor time courses. Bottom panel: results of applying the bDSSP algorithm to the sensor data in the top panel. Sensor time

courses in each panel are normalized to each maximum value, and the ordinate of the figure indicates the values normalized between −1 and 1.

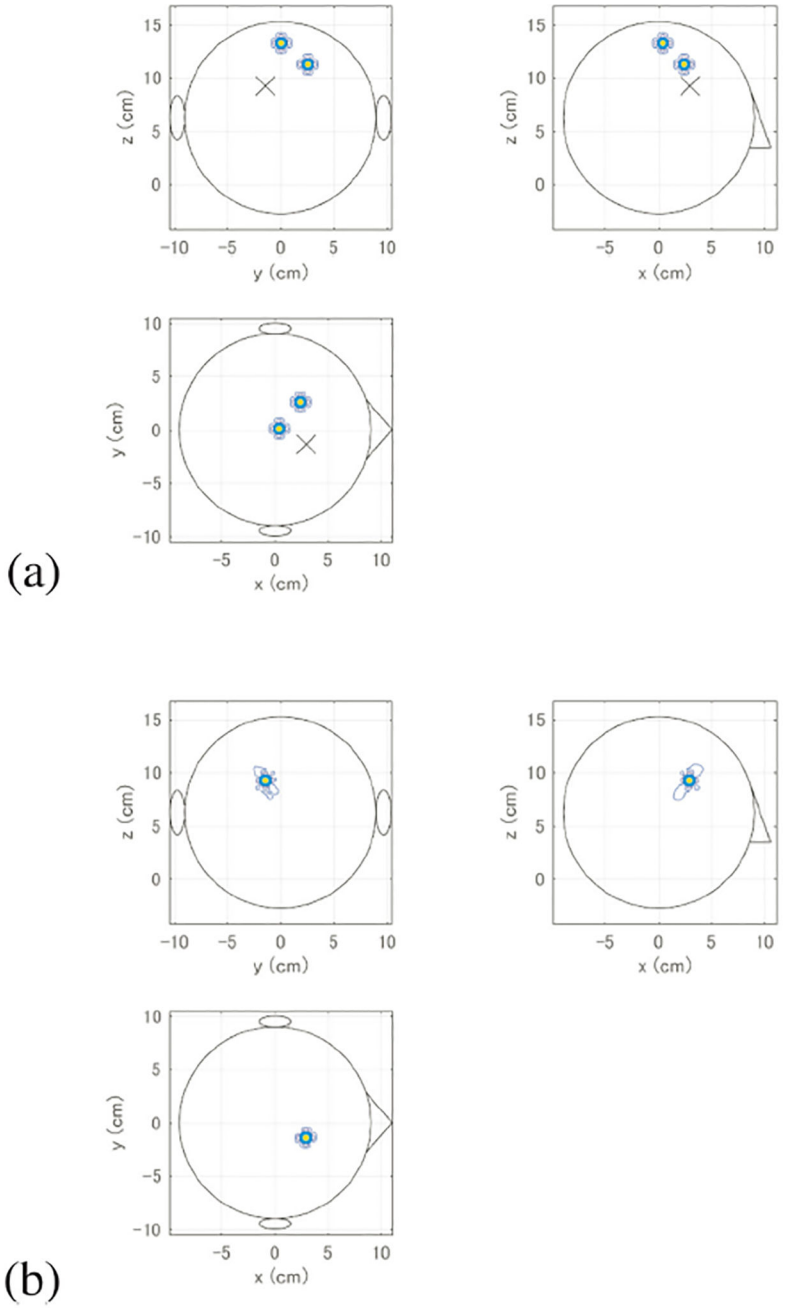

Figure 4.

(a) Source reconstruction results obtained using the simulated sensor time courses in the top panel of figure 3(b). The cross marks indicate the location of the deep source. (b) Source reconstruction results from the bDSSP-processed sensor data in the bottom panel of figure 3(b). In these results, the top left, top right and bottom panels, respectively, show the axial, coronal and sagittal projections of the 3D source reconstruction results.

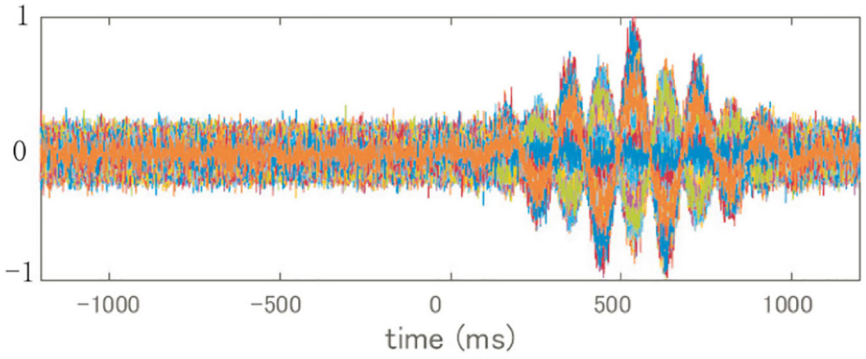

(a)

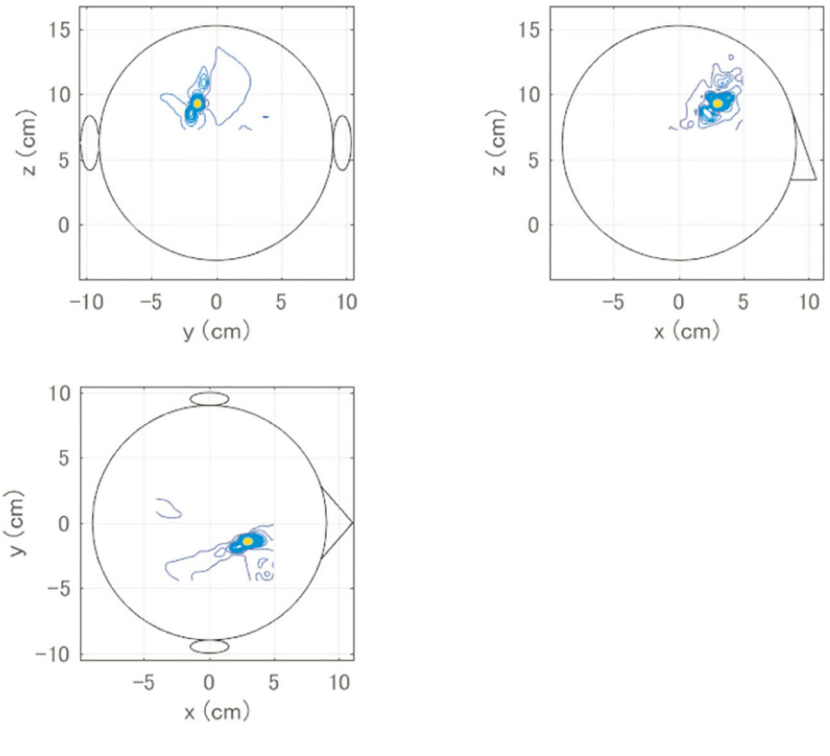

(b)

Figure 5.

(a) Results of applying the bDSSP algorithm to sensor data with SNR equal to 1.5. (The SNR is defined as $\|\boldsymbol{B}_{\text{deep}}\|_F/\|\boldsymbol{B}_{\boldsymbol{\varepsilon}}\|_F$) These sensor time courses are normalized between −1 and 1, and the ordinate indicates the normalized values. (b) Source reconstruction results obtained from the bDSSPprocessed sensor data in (a). In these results, the top left, top right and bottom panels, respectively, show the axial, coronal and sagittal projections of the 3D source reconstruction results.

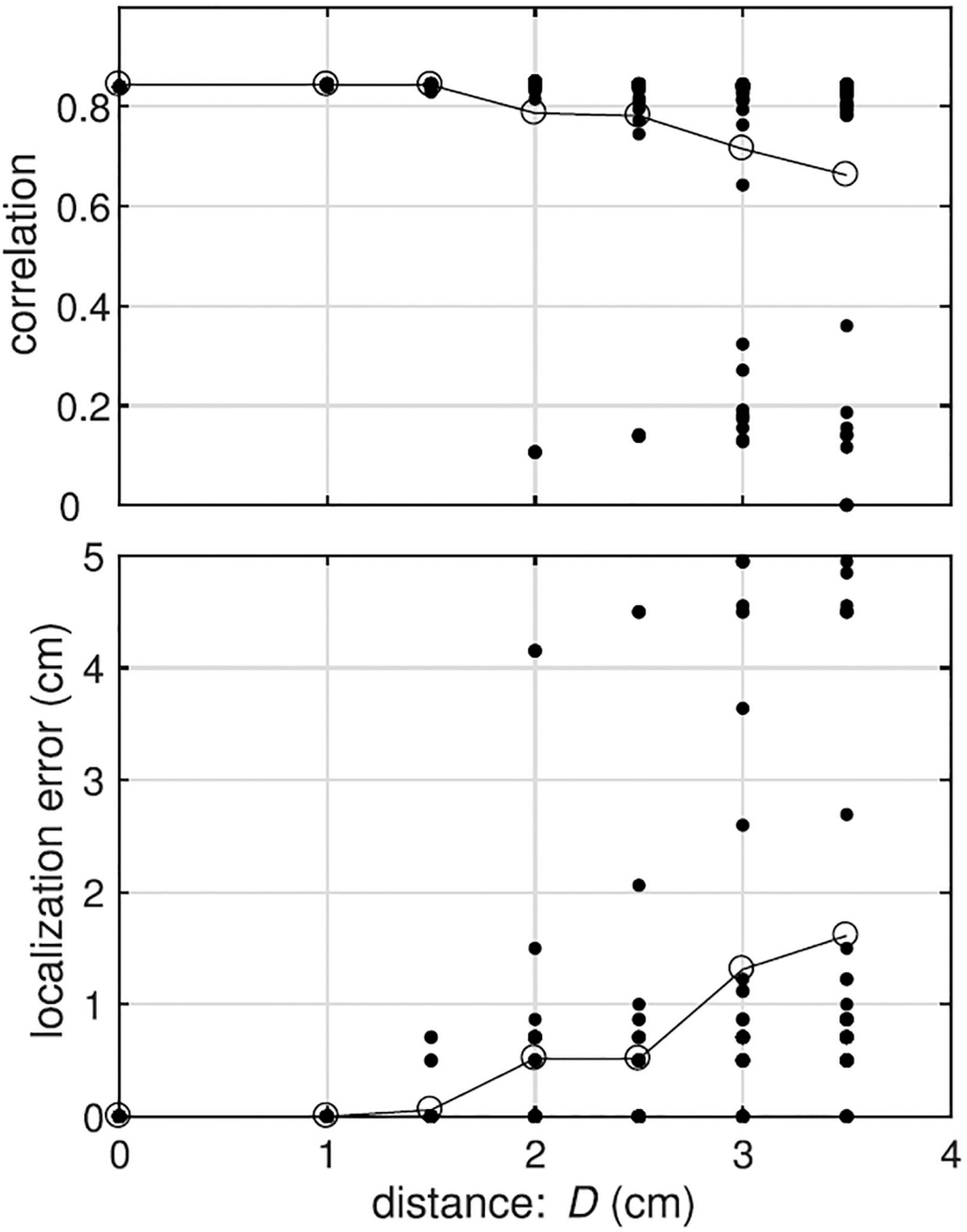

Figure 6.

Results of Monte Carlo experiments on the mismatch between the position of the local source space and the location of the target deep source. Top panel: plots of the sensor-time course correlation Φ versus the mismatch distance D. Bottom panel: plots of the localization error of the deep source versus D. The position of the local source space was set at fifty different locations having the same D. A filled dot represents the results of each Monte Carlo trial, and blank circles indicate the average of the Monte Carlo results at each D.

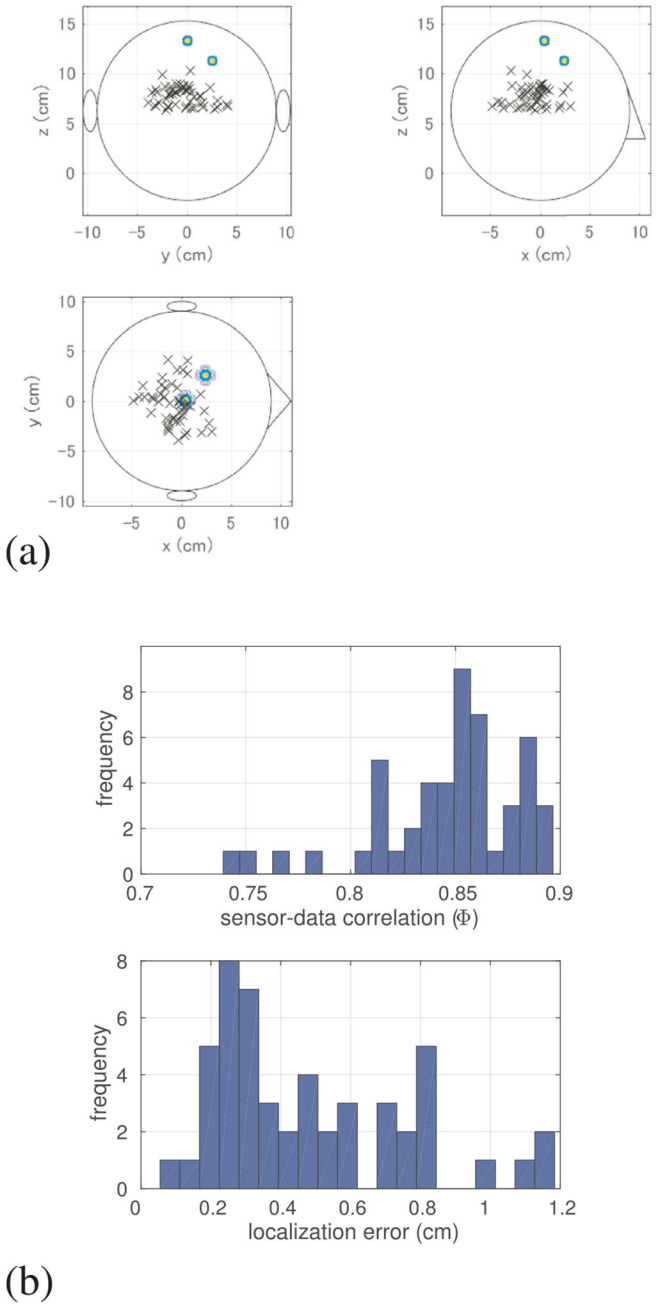

Figure 7.

Results of Monte Carlo experiments on the robustness of the bDSSP algorithm to the source configuration. (a) One hundred randomly-selected locations of the deep source generated in this Monte Carlo study. Each location is shown by a cross mark. Two blank circles show the locations of the superficial sources, which are the same as those used in the previous experiments. (b) Top panel: histogram of the one-hundred trials with respect to the sensor time course correlation Φ. Bottom panel: histogram of the one-hundred trials with respect to the source localization errors. In this study, SIR was set at 0.05, and SNR was set at 4.5.

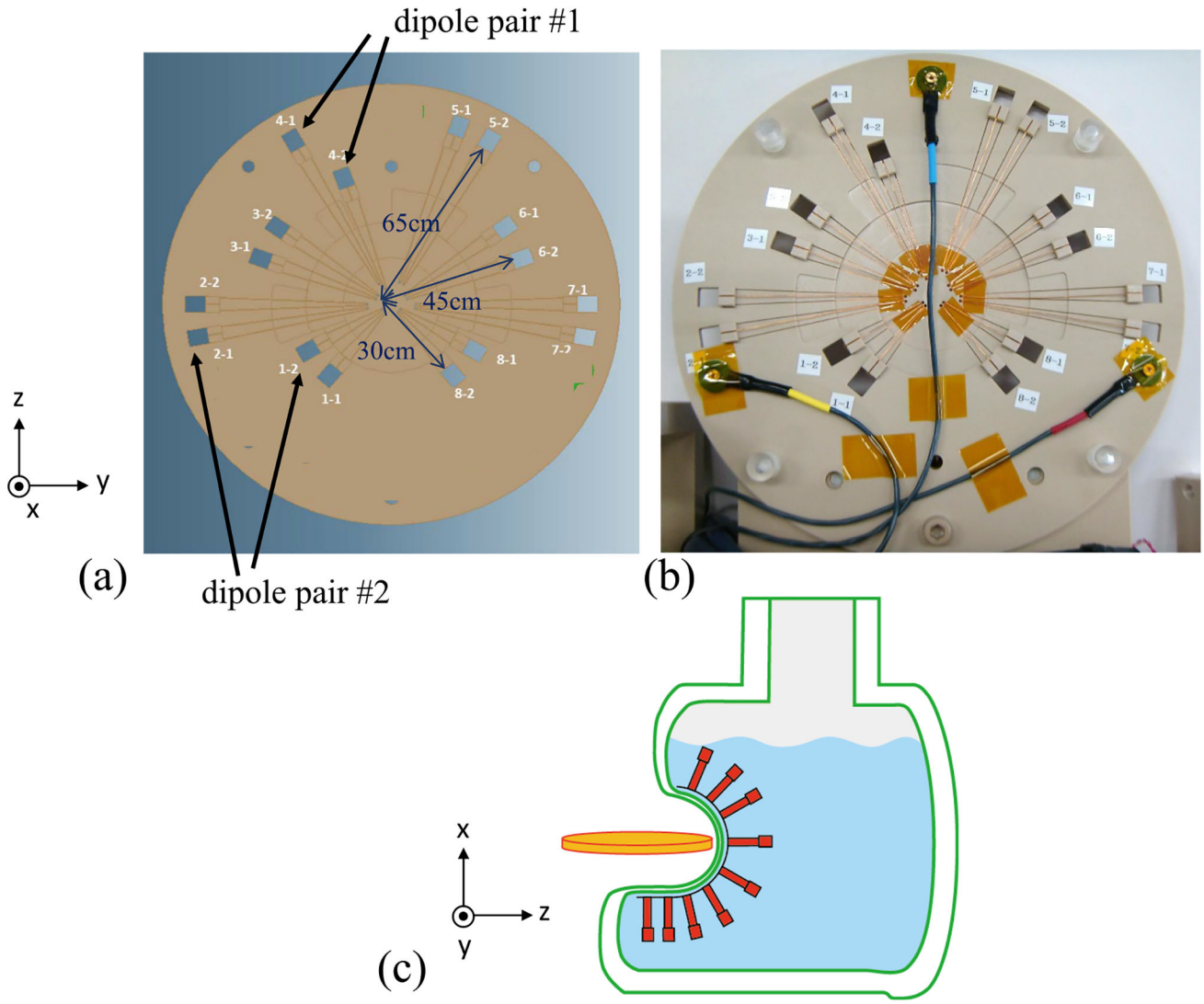

Figure 8.

Configuration of a dry phantom used in our experiments. (a) The squares show the locations of dipole sources. Dipole pairs annotated by ‘dipole pair#1’ and ‘dipole pair#2’ were those used in our experiments. Dipole pair#1 consists of dipole 4–1 and dipole 4–2, and the orientations of these dipoles are perpendicular to each other. Dipole pair#2 consists of dipole 2–1 and dipole 1–2, and the orientations of these dipoles are parallel. The center of the disc matches the sphere origin of the spherical conductor. (b) Isosceles-triangular-shaped coils that simulate dipole sources in the spherical homogeneous conductor can be seen. (c) Depiction showing how the disc-shaped phantom was installed inside the sensor helmet.

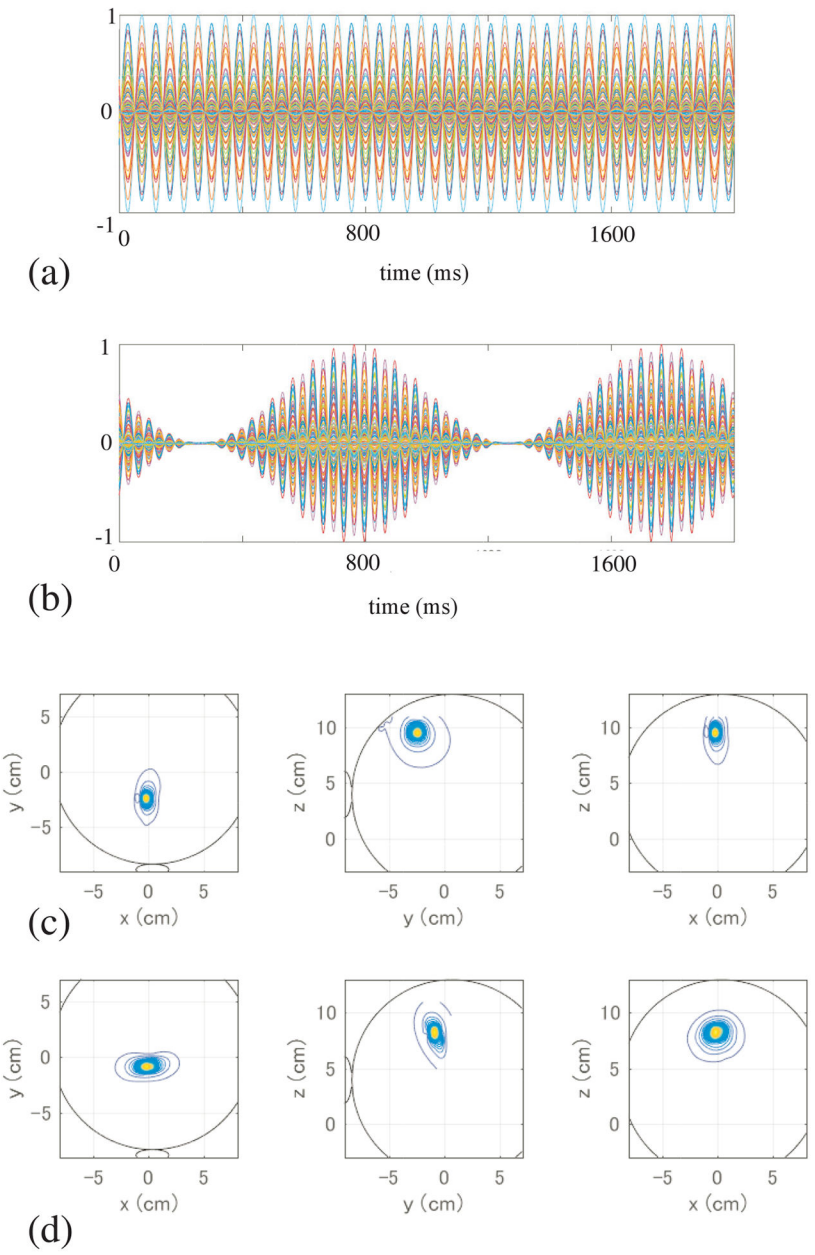

Figure 9.

(a) Sensor time courses measured when only the superficial dipole (marked ‘4–1’ in figure 8(a)) was active. The superficial dipole was driven by an 11 Hz sinusoid. (b) Sensor time courses measured when only the deep dipole (marked ‘4–2’ in figure 8(a)) was active. The deep dipole was driven with an amplitude-modulated sinusoid whose carrier frequency was 15 Hz and modulation frequency was 1 Hz. These sensor time courses in (a) and (b) are normalized to each maximum field intensity. The abscissa of these figures indicates time in ms. (c) Source reconstruction results of the superficial dipole. (d) Source reconstruction results of the deep dipole. In each figure, the left, middle, and right panels, respectively, show the axial, coronal and sagittal projections of the 3D source reconstruction results.

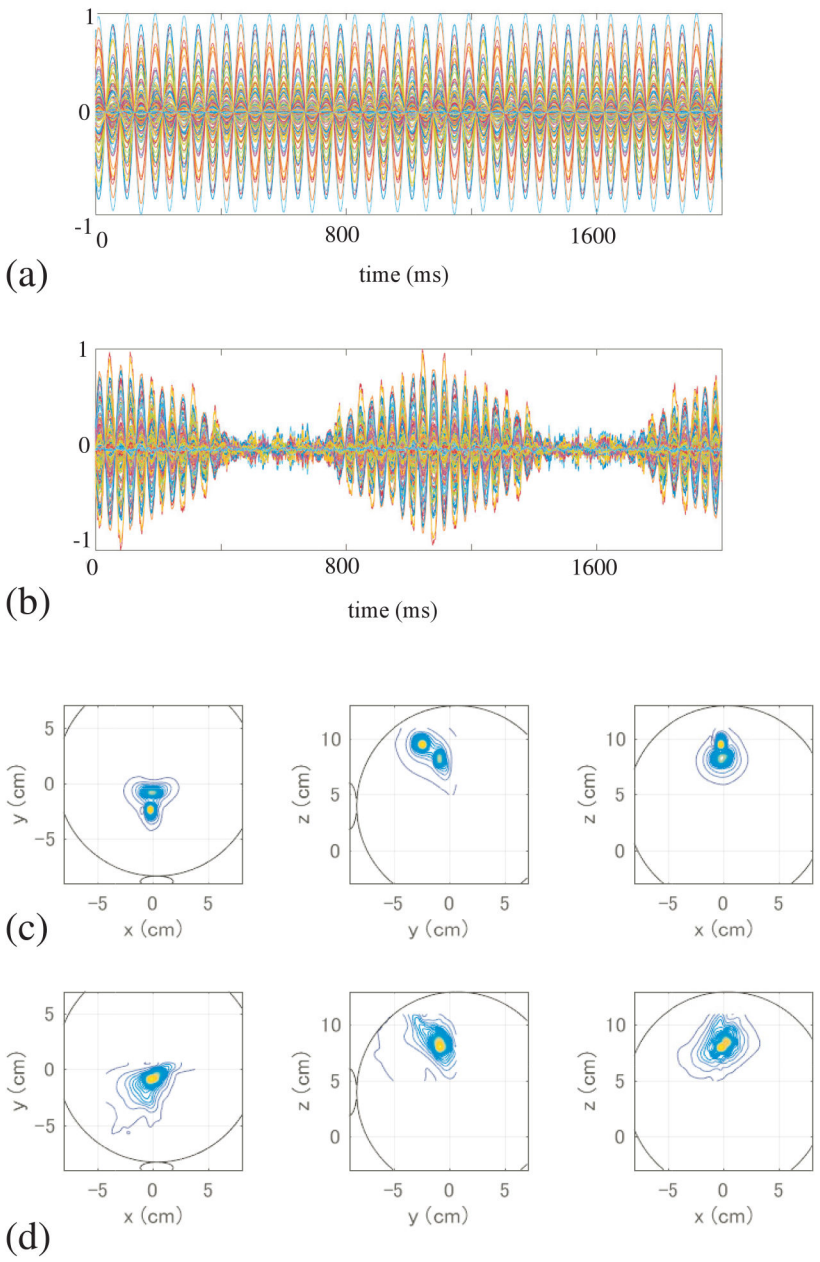

Figure 10.

(a) The sensor time courses measured when the superficial and deep dipoles were simultaneously active. The magnetic field from the superficial dipole was sixteen times stronger than the magnetic field from the deep dipole. (b) The sensor time courses of the bDSSP results. These sensor time courses in (a) and (b) are normalized to each maximum field intensity. The abscissa of these figures indicates time in ms. (c) Source reconstruction results from the sensor data in (a). (d) Source reconstruction results from the bDSSP-processed sensor data in (b). The left, middle, and right panels, respectively, show the axial, coronal and sagittal projections of the 3D source reconstruction results.

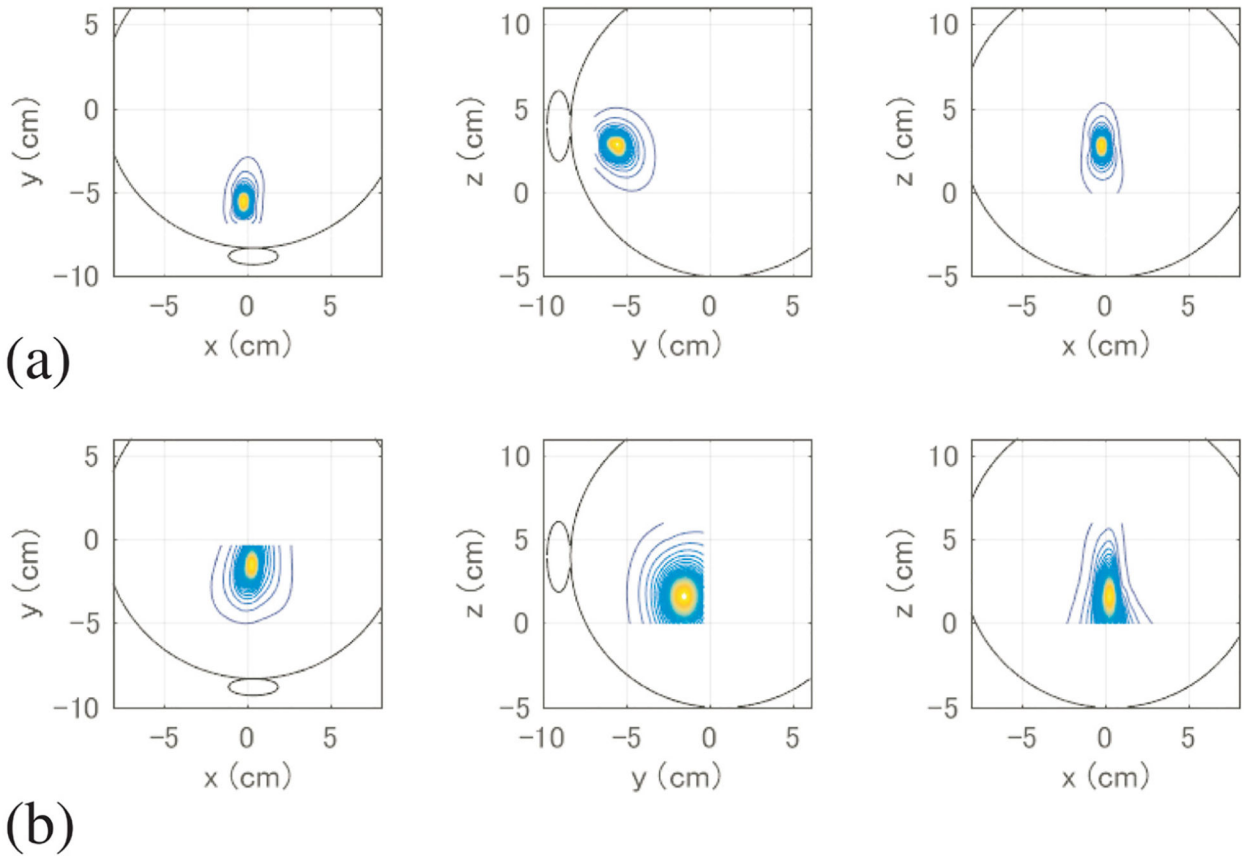

Figure 11.

Results of experiments using a pair of dipoles denoted ‘Dipole pair#2’; the deep dipole is denoted ‘2–1’, and the superficial dipole ‘1–2’. (a) The reconstruction results of the superficial dipole. (b) The reconstruction results of the deep dipole. The left, middle, and right panels, respectively, show the axial, coronal and sagittal projections of the 3D source reconstruction results.

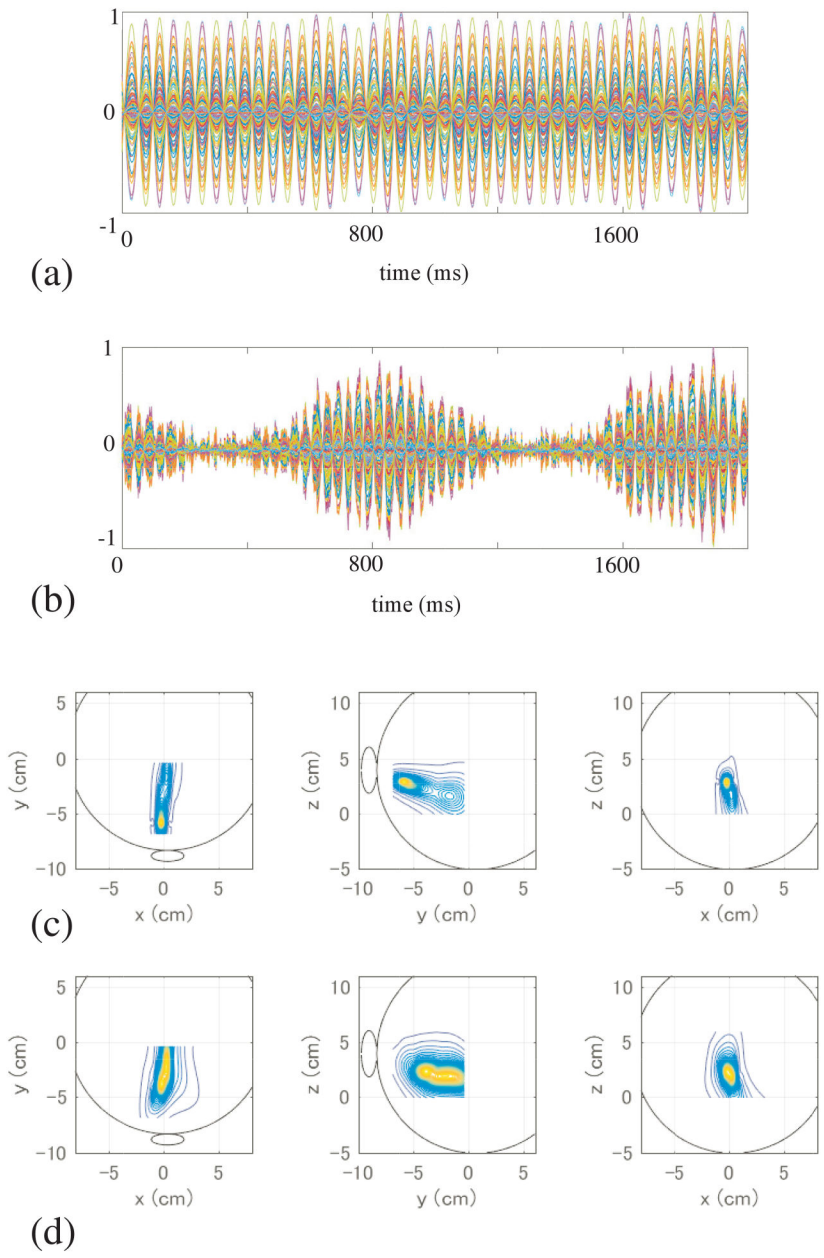

Figure 12.

Results of experiments using a pair of dipoles denoted ‘Dipole pair#2’; the deep dipole is denoted ‘2–1’, and the superficial dipole ‘1–2’. (a) The sensor time courses measured when the superficial and deep dipoles were simultaneously active. (b) The bDSSP-processed sensor time courses. These sensor time courses in (a) and (b) are normalized to each maximum field intensity. The abscissa of these figures indicates time in ms. (a) Source image reconstructed using the sensor data in (a). (b) Source image reconstructed using the bDSSP-processed sensor data in (b). The left, middle, and right panels, respectively, show the axial, coronal and sagittal projections of the 3D source reconstruction results.

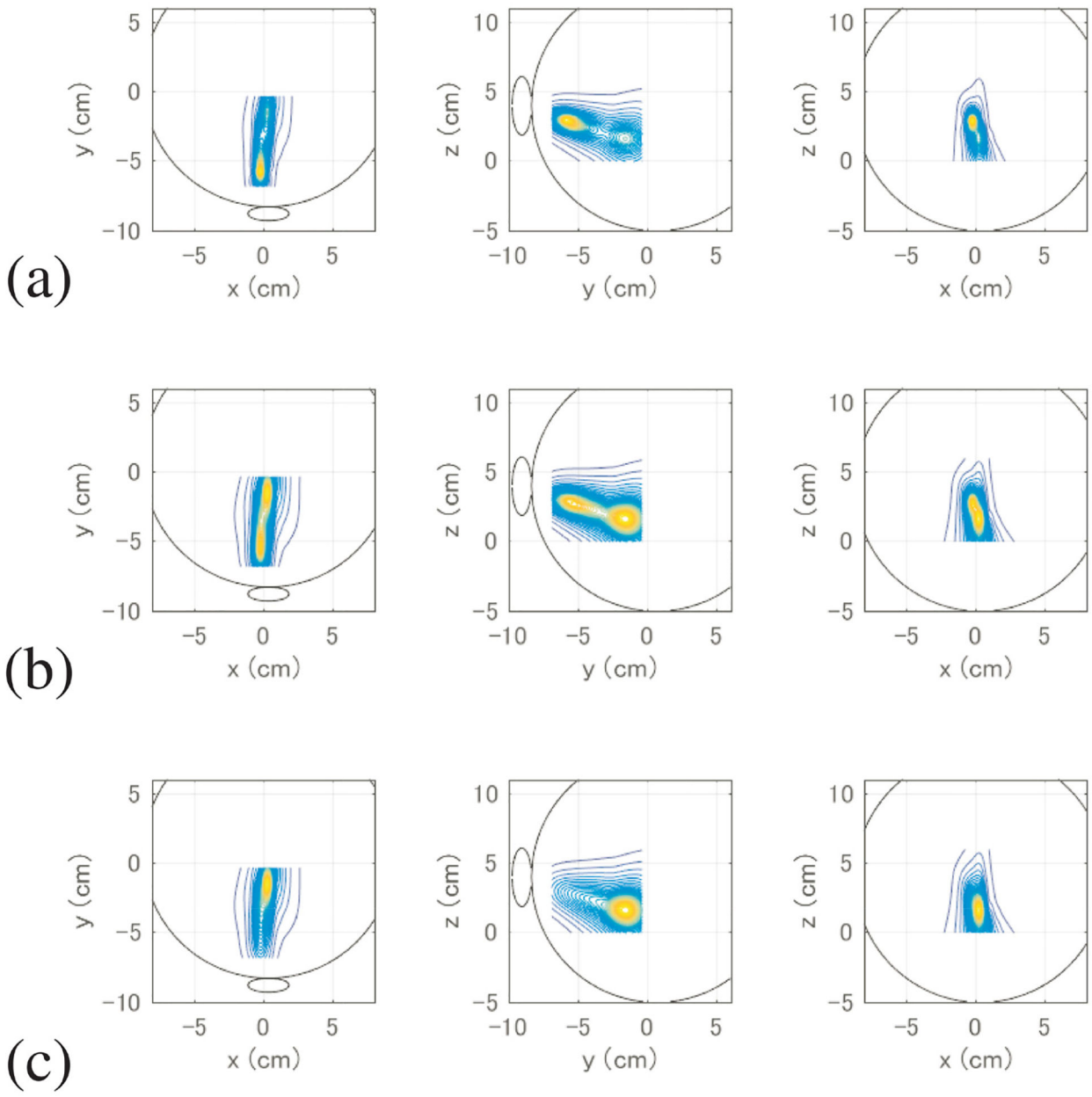

Figure 13.

Source reconstruction results obtained from synthetic sensor data $\boldsymbol{y}_{\mathbf{sy}}(t)$ obtained such that $\boldsymbol{y}_{sy}(t) = \boldsymbol{y}_{\text{deep}}(t) + \alpha \boldsymbol{y}_{\text{sup}}(t)$. Here, $\boldsymbol{y}_{\text{deep}}(t)$ is the sensor data measured when only the deep dipole (dipole'1–2') was active, and $\boldsymbol{y}_{\text{sup}}(t)$ is the sensor data measured when only the superficial dipole (dipole'2–1') was active. (a) Source reconstruction results when $\alpha = 0.04$. (b) Source reconstruction results when $\alpha = 0.02$. (c) Source reconstruction results when $\alpha = 0.01$.

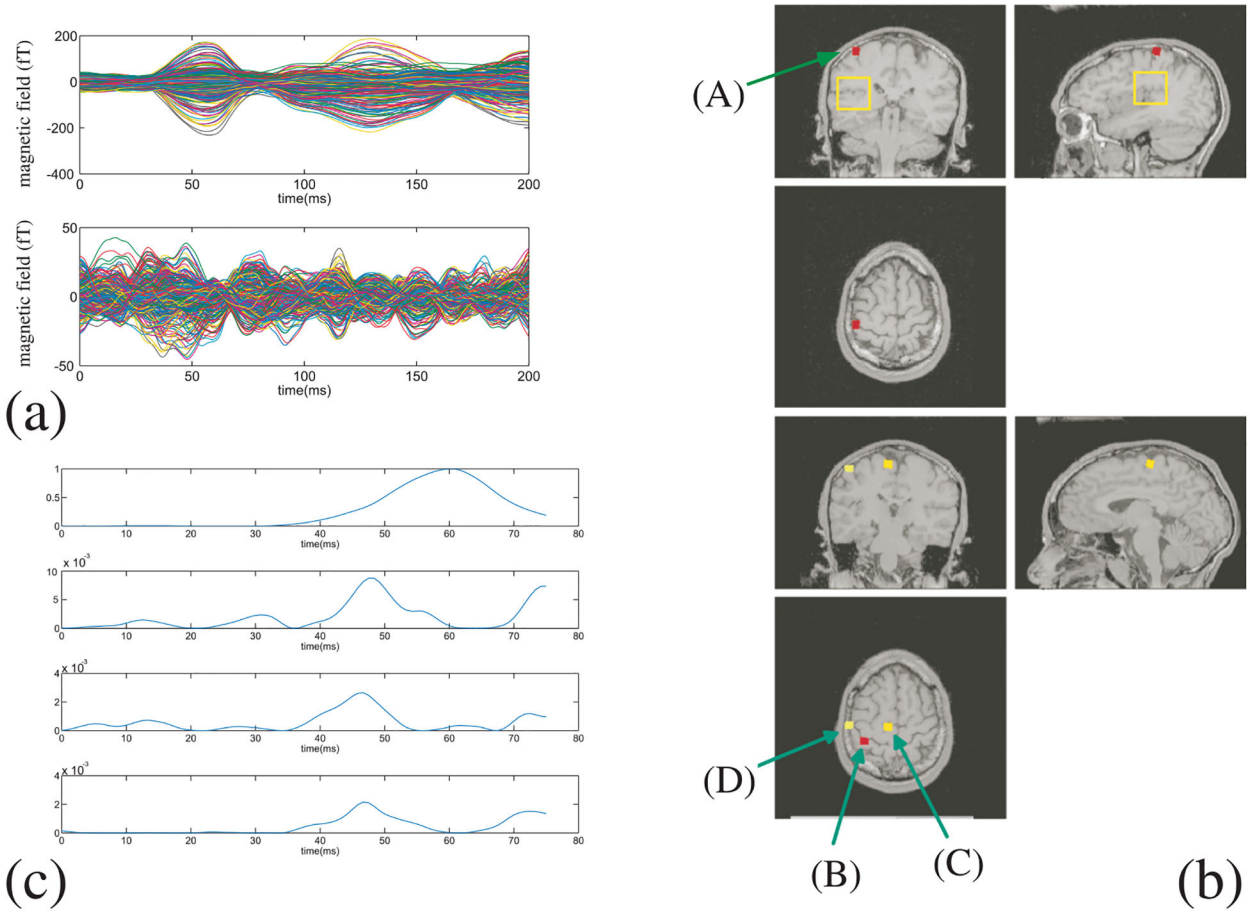

Figure 14.

(a) Top panel: somatosensory MEG data averaged across 240 trials collected using the 275-channel CTF MEG scanner. Bottom panel: the sensor time courses of the bDSSP results. (b) Top panel: results of source reconstruction obtained from the sensor data in the top panel of (a). The blank squares show the boundary of the local source space used when applying the bDSSP algorithm. A single source, labelled by (A), was detected at the primary somatosensory area. Bottom panel: results of source reconstruction obtained from the bDSSP-processed sensor data shown in the bottom panel of (a). Three sourses, labelled as (B)–(D), are detected. The cross sectional MR images were chosen as those at the voxel having the maximum intensity. (c) Reconstructed source time courses. The top, second top, third top, and bottom panels respectively show the time courses of voxels indicated by (A)–(D). The all four time courses are normalized to a common value equal to the maximum value of the time course in the top panel.

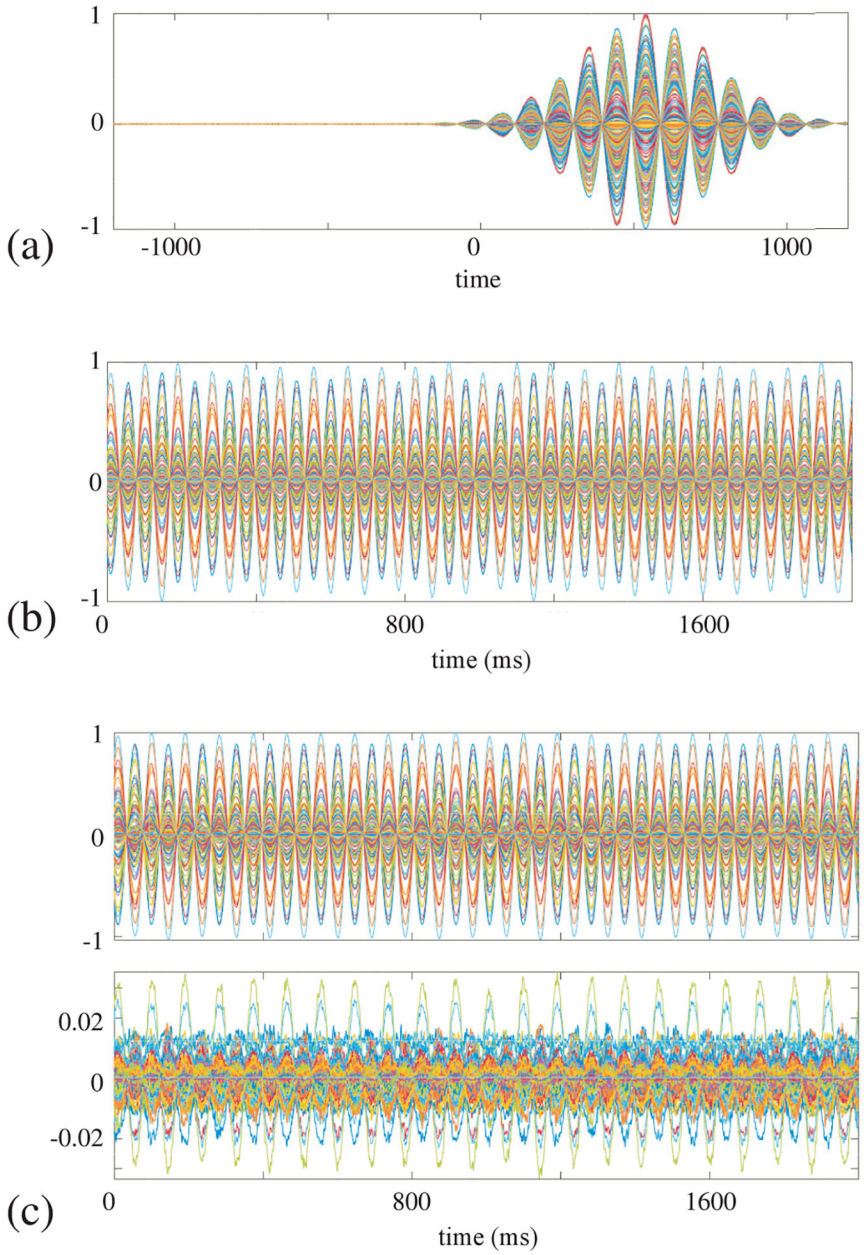

Figure 15.

(a) Results of applying the cbDSSP algorithm to the computer generated data in the top panel of figure 3(a). (b) Results of applying the cbDSSP algorithm to the phantom data in figure 10(a) obtained using dipole pair#1. The sensor time courses in (a) and (b) are normalized to each maximum value, and the ordinate of these figures indicates the normalized values of the magnetic field intensity. (c) Two data sets, $\boldsymbol{P}_{\text{sup}}\boldsymbol{B}$ and $(\boldsymbol{I} - \mathbf{P}_{\text{sup}})\boldsymbol{B}$, from the phantom data, obtained using dipole pair#1. The data set $\boldsymbol{P}_{\text{sup}}\boldsymbol{B}$ is shown in the upper panel and the data set $(\boldsymbol{I} - \boldsymbol{P}_{\text{sup}})\boldsymbol{B}$ is in the lower panel. These data sets are normalized to the same maximum value of $\boldsymbol{P}_{\text{sup}}\boldsymbol{B}$.

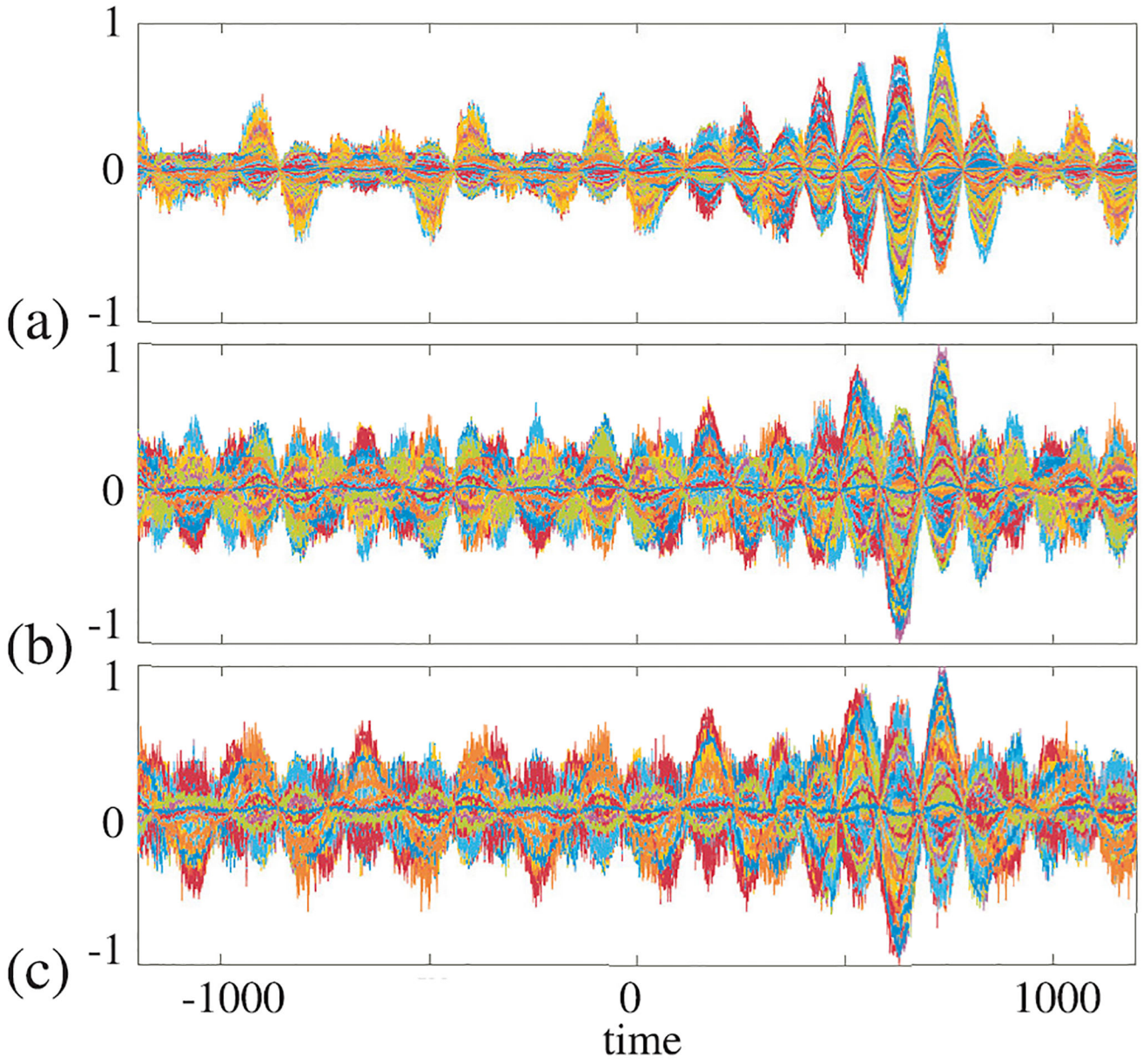

Figure 16.

(a) Results of applying the beamspace SSS method to simulated sensor measurements in the top panel of figure(a). (a) Results obtained with L_T set at 1. (b) Results obtained with L_T set at 2. (c) Results obtained with L_T set at 3. These sensor time courses in (a)–(c) are normalized to each maximum field intensity.

Table 1.

Source properties assumed in computer simulation.

Source number	Orientation	Location (cm)	Distance from the sphere origin (cm)
1	(1,−1, 0)	(0.4, 0.1, 13.3)	7.0
2	(0, 1, 1)	(2.9, −1.4, 9.3)	4.4
3	(1, 0, 1)	(2.4, 2.6, 11.3)	6.1